INFORMATION TO USERS

This manuscript has been reproduced from the microfilm master. UMI films the text directly from the original or copy submitted. Thus, some thesis and dissertation copies are in typewriter face, while others may be from any type of computer printer.

The quality of this reproduction is dependent upon the quality of the copy submitted. Broken or indistinct print, colored or poor quality illustrations and photographs, print bleedthrough, substandard margins, and improper alignment can adversely affect reproduction.

In the unlikely event that the author did not send UMI a complete manuscript and there are missing pages, these will be noted. Also, if unauthorized copyright material had to be removed, a note will indicate the deletion.

Oversize materials (e.g., maps, drawings, charts) are reproduced by sectioning the original, beginning at the upper left-hand corner and continuing from left to right in equal sections with small overlaps.

ProQuest Information and Learning
300 North Zeeb Road, Ann Arbor, MI 48106-1346 USA
800-521-0600

ACCELERATED ALGORITHMS AND UNIVERSALITY IN COARSENING SYSTEMS

by

Mowei Cheng

SUBMITTED IN PARTIAL FULFILLMENT OF THE
REQUIREMENTS FOR THE DEGREE OF
DOCTOR OF PHILOSOPHY

AT

DALHOUSIE UNIVERSITY
HALIFAX, NOVA SCOTIA
AUGUST 2005

DALHOUSIE UNIVERSITY

To comply with the Canadian Privacy Act the National Library of Canada has requested that the following pages be removed from this copy of the thesis:

Preliminary Pages

Examiners Signature Page (pii)

Dalhousie Library Copyright Agreement (piii)

Appendices

Copyright Releases (if applicable)

To Hongye

Table of Contents

List of Tables

List of Figures

List of Symbols

$\phi(\mathbf{x}, t)$	Order parameter
L_{sys}	Linear system size
Δx	Lattice spacing
N	Linear lattice size, $N = L_{sys}/\Delta x$
Δt	Algorithmic time-step
Δt_{Eu}	Fixed Euler time-step
Δt_s	Structural time-step
$L(t)$	Characteristic length
ξ	Interfacial width
Δt_{eff}	Fourier-space effective time-step
t_s	Structural time
Δt_{nat}	Natural time-step
μ	Chemical potential
σ	Surface tension
$E(t)$	Energy density
$F[\phi]$	Free energy
$C(\mathbf{r}, t)$, $S(\mathbf{k}, t)$	Correlations
$C(r, t)$, $S(k, t)$	Spherically averaged correlations
$f(r/L)$, $g(kL)$	Scaled time-independent correlations
$T(\mathbf{k}, t)$	Time-derivative correlations in Fourier-space
$h(kL)$	Scaling function of time-derivative correlations
a_1, a_2	Direct parameterization
α	Growth exponent
$\Delta\tilde{\phi}^s$	Single-step error compared with exact dynamics
$\Delta\tilde{\phi}^m$	Bound of multi-step error compared with exact dynamics
$\lambda_{\mathbf{k}}$	Fourier-transformed Laplacian
$M(\phi)$	Order-parameter-dependent mobility
$M_{\pm}$	Asymmetric bulk mobilities

$\tilde{\phi}(\mathbf{x}, t + \Delta t)$	Order parameter updated by semi-implicit equations
A	Prefactor used in accelerated algorithms in conserved dynamics
B_{CO}, B_{NC}	Prefactors used to define structural time t_s using energy density E

Abstract

The first part of this thesis (Chapters 1 – 4) addresses accelerated algorithms for coarsening systems — we review unconditionally stable algorithms for the study of coarsening systems with a conserved or non-conserved scalar order parameter. These algorithms allow us to take arbitrarily large time-steps constrained only by desired accuracy. For conserved coarsening systems, these accelerated algorithms provide maximally-fast numerical algorithms — we can actually use the natural time-step $\Delta t = At_s^{2/3}$. To study the accuracy we compare the scaling structure obtained from our maximally-fast conserved systems directly against the standard fixed-time-step Euler algorithm, and find that the error is time-independent in the scaling regime and scales as $\sqrt{A}$ — this is consistent with an approximate bound of the error. Arbitrary accuracy is accessible for these maximally driven coarsening algorithms. These algorithms provide the most efficient and accurate means to reach the scaling regime for large systems. For non-conserved systems, however, with these accelerated algorithms, only effectively finite time-steps are accessible. The maximal time-step obtained by these algorithms is about four times the time-step of the Euler algorithm.

The second part of this thesis (primarily Chapter 5) applies these accelerated algorithms to the study of universality classes of scaled correlations in coarsening systems. Specifically, we study the universality classes found by introducing asymmetric bulk mobilities. We also develop accelerated algorithms for the study of systems with anisotropic surface tension.

Acknowledgements

I thank my thesis supervisor, Prof. Andrew Rutenberg, for his guidance, support, encouragement and patience in my PhD study. I have benefited greatly from the good collaborative environment in his group. His philosophy of "doing better" is always a great motivation of doing better research.

I thank the members of the supervisory committee Profs. Hans Jurgen Kreuzer, Manfred Jericho and Ian Folkins for their valuable suggestions and input in my PhD study.

I have enjoyed the friendly environment in Department of Physics and Atmospheric Science at Dalhousie University, which helped to make my PhD study fruitful.

I thank Nikolas Provatas, Hans Jurgen Kreuzer, Manfred Jericho, Andrew Rutenberg, Jun Allard, Gillian Ryan, Benjamin Downing and Alison Hill for asking interesting questions related to this thesis. I have gained better understanding from their questions.

A special thank goes to Jun Allard for kindly proofreading this thesis.

Finally, I thank my wife Hongye and daughter Sylvia, without whose unconditional love and support this thesis would not be possible.

Chapter 1

Introduction

This Chapter contains an introduction of some basic topics that related to the thesis, and a précis of the thesis.

1.1 Phase ordering dynamics

The theory of phase-ordering dynamics or "coarsening" has a history of more than three decades. For reviews, see Bray [1], Gunton *et al.* [2], Furukawa [3] and Langer [4]. Examples are found in the non-equilibrium coarsening of polymer mixtures [5], alloys [6, 7], liquid-crystals [8, 9], and in cosmology [10].

Phase ordering dynamics studys a system quenched from a high temperature disordered phase into a low temperature ordered phase, after which a complicated domain structure develops. A simple example is found in the two-dimensional Ising system under spin-exchange or spin-flip dynamics, where the spins can be either $+1$ or -1, and can only interact with the nearest neighbors. We look at what happens when it is cooled rapidly under T_c from a disordered state. At time $t = 0$ we make a temperature quench from an initial temperature $T_I > T_c$ to a final temperature $T_F < T_c$ (see Fig.1.1 and Fig.1.3).

As time proceeds, we will see "domain coarsening" — domain structure coarsens and the average size of the domain grows by continuously reducing the amount of the domain walls (see Fig.1.2). After the quench, the system is not in equilibrium — the experimental observation is that a pattern of domains of the equilibrium phase develops and as the time t increases the length scale of these regions grows. The later stage of this phase ordering process is believed to show universal scaling behavior: it is found that the dynamics are dominated by a single length scale, the domain size $L(t)$, which increases with a power law in time, $L(t) \sim t^{\alpha}$. The patterns at different time scales are statistically similar, apart from a global change of length scale at different

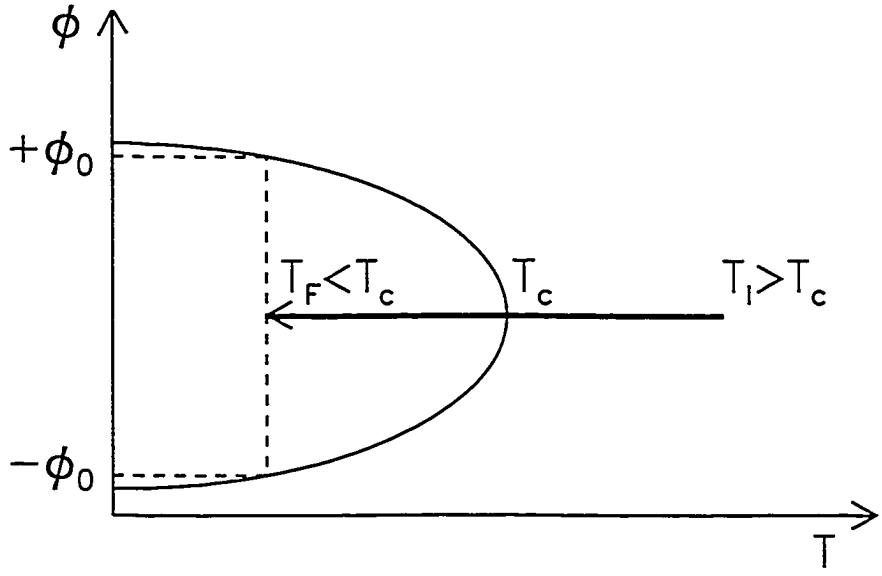

Figure 1.1: The phase diagram of an Ising model in zero applied field (schematic) to illustrate a temperature quench at time $t = 0$. The arrow indicates a quench from $T_I > T_c$ in the disordered phase to $T_F < T_c$ in the ordered phase where there are two degenerate equilibrium state $\pm\phi_0$.

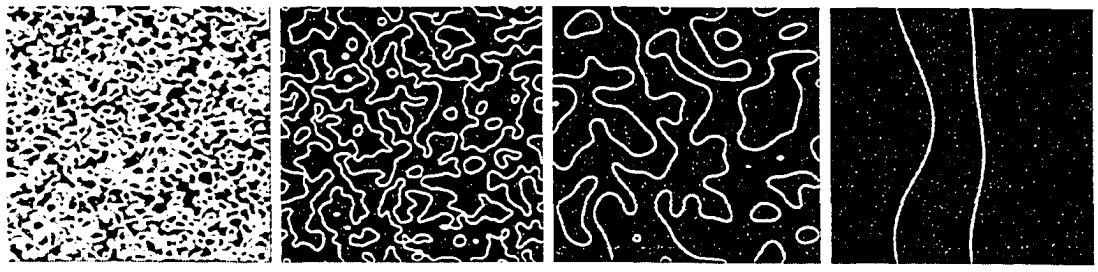

Figure 1.2: Typical snapshots of coarsening simulation for the non-conserved system with $L_{sys} = 256$ at times $t = 4.3$, 12.9, 67.8 and 4095.3, with a direct update ($a_1 = 3$, $a_1 = 0$). The left one represents the transient period, the middle two are in scaling regime, and the right one shows strong finite-size effects (see Appendix B).

times. For non-conserved scalar order parameter, $\alpha = 1/2$, and for conserved scalar order parameter, $\alpha = 1/3$ [1].

1.2 Dynamical models

To study coarsening, we first need a description in terms of an order parameter field $\phi(\mathbf{x}, t)$. A suitable Ginzburg-Landau free energy functional to describe the ordered phase is

$$F[\phi] = \int d^2x \left[\frac{1}{2}(\nabla\phi)^2 + V(\phi)\right], \tag{1.1}$$

where the potential $V(\phi)$ has a double-well structure (see Fig.1.3):

$$V(\phi) = \frac{(\phi^2 - 1)^2}{4}. \tag{1.2}$$

This is used throughout this thesis, though with modifications in Chapter 5. We choose $V(\phi)$ so that the minima occur at $\phi = \pm 1$, and $V(\pm 1) = 0$. The two minima of V correspond to the two equilibrium phases $\phi = \pm 1$, while the gradient-squared term in Eq.(1.1) associates an energy cost to an interface between the phases.

When the order parameter is conserved under the dynamics, our equation of motion can be written in the form of a continuity equation,

$$\frac{\partial\phi}{\partial t} = -\nabla \cdot \mathbf{j}, \tag{1.3}$$

with current

$$\mathbf{j} = -M_0 \nabla\mu. \tag{1.4}$$

where M_0 is the mobility and μ is the local chemical potential defined by

$$\mu \equiv \frac{\delta F}{\delta\phi} = -\nabla^2\phi + \frac{dV}{d\phi} = -\nabla^2\phi - \phi + \phi^3. \tag{1.5}$$

Absorbing M_0 into the time scale, we obtain the dimensionless form

$$\frac{\partial\phi}{\partial t} = -\nabla^2(\nabla^2\phi + \phi - \phi^3). \tag{1.6}$$

Eq.(1.6) is often called the Cahn-Hillard (CH) equation [12]. In this thesis, this equation describes "conserved dynamics".

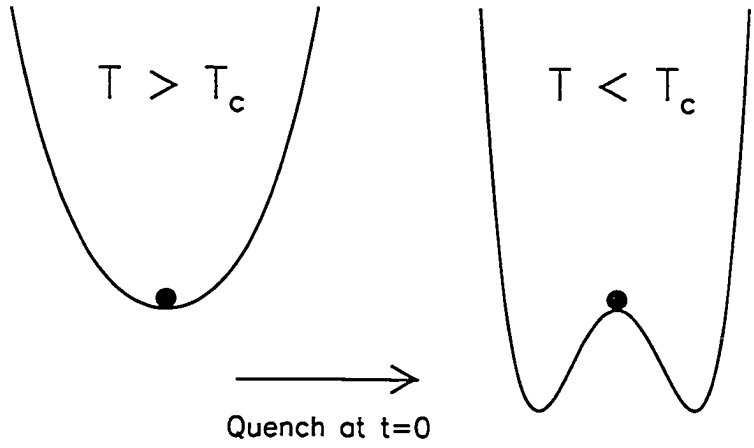

Figure 1.3: Plot of potentials $V(\phi)$ vs ϕ before and after the quench. As the system is quenched from an initial temperature $T_I > T_c$ to a final temperature $T_F < T_c$, the potential goes from having a single minimum at $\phi = 0$ to having two global minima at $\phi = \pm\phi_0$. As a result, locally, the system must choose either $+\phi_0$ or $-\phi_0$ (see Eq.(1.2)).

In the case where the order parameter is not conserved by the dynamics, the simplest dissipative equation for the time evolution of the field ϕ is

$$\frac{\partial \phi}{\partial t} = -\mu = \nabla^2 \phi + \phi - \phi^3. \tag{1.7}$$

Eq.(1.7) describes that the rate of change of ϕ is proportional to the gradient of the free-energy functional in functional space, and is often called the Time-Dependent-Ginzburg-Landau (TDGL) equation [1]. In this thesis, this equation describes "non-conserved dynamics".

In the late time scaling regime, the characteristic length scale $L(t)$ is large compared to the interfacial width ξ and the equilibrium correlation length, the thermal fluctuations become unimportant and the system behaves as if it were at $T = 0$ according to a renormalization group (RG) study [1, 11]. Therefore we have ignored the noise terms in Eq.(1.6) and Eq.(1.7).

1.3 Domain walls

Following Bray [1], if we look at the equilibrium interface profile (for a flat and therefore stationary interface), from Eq.(1.7), the wall profile (see Fig.1.4) is the solution of

$$\mu = \frac{dV}{d\phi} - \frac{d^2\phi}{dg^2} = 0 \tag{1.8}$$

with boundary condition $\phi(\pm\infty) = \pm 1$, where g is a coordinate normal to the wall. Without loss of generality, we let $\phi(0) = 0$. Multiplying by $d\phi/dg$ on both side, integrating, and imposing the boundary conditions, gives

$$\left(\frac{d\phi}{dg}\right)^2 = 2V(\phi) = \frac{(\phi^2-1)^2}{2}, \tag{1.9}$$

which is solved by

$$\phi(g) = \tanh\left(\frac{g}{\sqrt{2}}\right), \tag{1.10}$$

which implies that a natural interfacial width $\xi \approx 2\sqrt{2}$. This result can be used in Eq.(1.1) to give the free energy per unit area of wall, i.e. the surface tension, as

$$\sigma = \int_{-\infty}^{\infty} dg \left[\frac{1}{2}\left(\frac{d\phi}{dg}\right)^2 + V(\phi)\right], \tag{1.11}$$

$$= \int_{-1}^{1} d\phi \sqrt{2V(\phi)}, \tag{1.12}$$

$$= \frac{2\sqrt{2}}{3}, \tag{1.13}$$

where Eq.(1.9) is used. Note that in this calculation, the two terms in the free energy Eq.(1.1) contribute equally.

1.4 Dynamical scaling

The scaling hypothesis states that there exists, at late times, a single characteristic length $L(t)$ such that the domain structure is independent of time when lengths are scaled by $L(t)$. This hypothesis is supported by experiment [13] and numerical simulation [14]. Two commonly used probes of the domain structure are the equal-time pair correlation function

$$C(\mathbf{r},t) = \langle \phi(\mathbf{x}+\mathbf{r},t)\phi(\mathbf{x},t)\rangle, \tag{1.14}$$

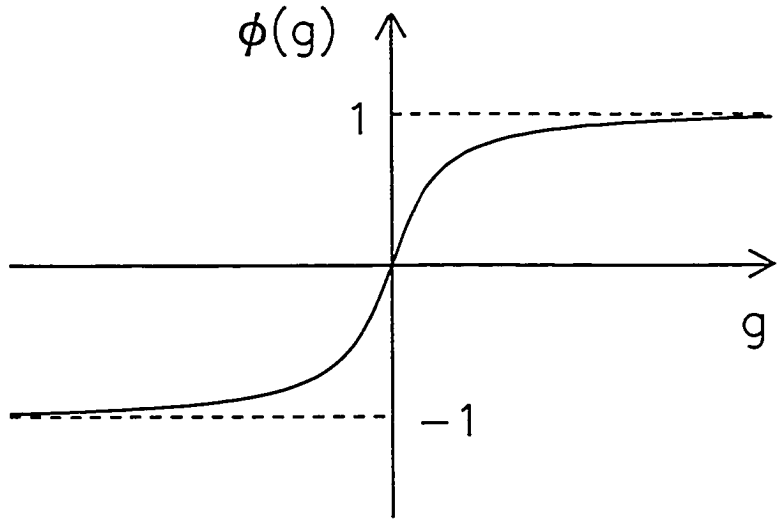

Figure 1.4: Domain wall profile function $\phi(g)$ (schematic, see Eq.(1.10)).

and its Fourier transform, the equal-time structure factor

$$S(\mathbf{k},t) = \langle \phi_{\mathbf{k}}(t)\phi_{-\mathbf{k}}(t)\rangle. \tag{1.15}$$

where $\phi_{\mathbf{k}}(t)$ is the Fourier transform of $\phi(\mathbf{x},t)$. Here angle brackets indicate an average over initial conditions. The existence of a single characteristic length scale, according to the scaling hypothesis, implies that at late times after the quench the pair correlation function and the structure factor have the scaling forms

$$C(\mathbf{r},t) = f\left(\frac{\mathbf{r}}{L}\right), \tag{1.16}$$

$$S(\mathbf{k},t) = L^2 g(\mathbf{k}L), \tag{1.17}$$

where the function g is the Fourier transform of the function f. We can measure the spatial scaling functions f and g and see if they are independent of time. On the other hand, we know that the energy density $E(t) \sim 1/L(t)$ (see Chapter 4 for details). Therefore, in two-dimensions, we obtain more convenient scaling form

$$f(\mathbf{r}E) \equiv C(\mathbf{r},t), \tag{1.18}$$

$$g\left(\frac{\mathbf{k}}{E}\right) \equiv S(\mathbf{k},t)E^2, \tag{1.19}$$

which are easy to measure numerically. These scaling forms are used in this thesis.

1.5 Universality classes of correlations

In the study of the equilibrium critical behavior of quantities such as the correlation length and specific heat near a critical temperature T_c, we encounter the concept of "universality class" [15] — the sets of all systems which have a given "universal" critical behavior such as the values of critical exponents and critical amplitude ratios. The critical behavior only depends on the spatial dimensionality d and the order parameter dimensionality n, but not on specific values of coupling constant, lattice type, or the precise form of the model Hamiltonian.

Universality classes are also exhibited in far-from-equilibrium phase ordering dynamics. As in equilibrium critical behavior, the lattice structure, initial conditions, and the average values of the order parameters are not important [1] in determining the growth exponents α for different systems. On the other hand, any conservation laws obeyed by the dynamics ($\mu = 0$ for non-conserved dynamics and $\mu = 2$ for conserved dynamics [16]), spatial dimensionality d and the order parameter dimensionality n ($n = 1$ for scalar order parameter and $n > 1$ for vector order parameter) are parameters that affect the scaling exponents.

The universality class of growth exponents are large ones — in two dimension, $\alpha = 1/3$ for conserved scalar order parameter, and $\alpha = 1/2$ for non-conserved scalar order parameter [1]. In this thesis, we will study a relatively small universality class — the universality class of correlations. The correlation function is an important quantity to characterize phase ordering dynamics, and is measured in both experiments and computer simulations. Spatial anisotropy of the surface tension has been shown to change the scaled correlations in the scaling regime but not growth exponents [36], and so represents an example of much smaller universality classes. Recently, there is some research showing that the different values of mobilities in the two equilibrium states will affect correlations shortly after the quench [17]. We investigate this system in the late time scaling regime in Chapter 5.

1.6 Précis

Throughout this thesis, all the systems we have studied are in two dimensions. Chapter 1 introduces the basic concepts including phase ordering dynamics, dynamical scaling and universality class. The numerical algorithms which have been used in phase ordering dynamics are discussed in Chapter 2 — we talk about the traditional Euler fixed-step algorithm, followed by discussion of some recent accelerated algorithms, and their drawbacks, then we introduce the algorithm proposed by Eyre, which is extended to our maximally-fast algorithms. Chapter 3 discusses the stabilities of numerical algorithms, including a von Neumann linear stability analysis and a numerical test for stability. This chapter also introduces the unconditionally stable algorithm that enables time-step $\Delta t \to \infty$ as $t_s \to \infty$. Chapter 4 contains the discussion of accuracy of these unconditionally stable algorithms in both conserved and non-conserved systems. The concepts of effective time-step and structural time-step will be introduced and analyzed here, together with some calculations. Chapter 5 applies these accelerated algorithms to investigate universality class of correlations on asymmetric bulk mobilities. Finally, in Chapter 6, there is a summary and a discussion of the work done so far and some perspective of the future work. The Appendices expand on some topics that are not discussed in detail in the body of the thesis.

Chapter 2

Numerical algorithms

The CH and TDGL equations introduced in Chapter 1 are non-linear partial differential equations that cannot generally be solved analytically for random (disordered) initial conditions. Therefore, computer simulations of the CH and TDGL equations play an essential role in our understanding and characterization of coarsening. In this Chapter, we will discuss numerical algorithms used to study coarsening systems with conserved (CH) or non-conserved (TDGL) order parameter.

2.1 Previous algorithms

The traditional Euler time-discretization of the TDGL equation Eq.(1.7) is

$$\phi^{Eu}_{t+\Delta t} \equiv \phi_t - \Delta t \mu_t, \tag{2.1}$$

and

$$\phi^{Eu}_{t+\Delta t} \equiv \phi_t + \Delta t \nabla^2 \mu_t \tag{2.2}$$

for the CH equation, where

$$\mu_t = -\nabla^2 \phi_t - \phi_t + \phi_t^3. \tag{2.3}$$

Euler updates are "explicit" since the field at the earlier time (ϕ_t) explicitly determines the field at the next step ($\phi_{t+\Delta t}$). The standard Euler integration of the CH and TDGL equations is known to be unstable for time step Δt above a threshold (see Appendix A and [19]). This forces the use of a fixed time step irrespective of the natural time scale of the dynamics. Meanwhile, the motion of the domain walls becomes extremely slow at late times after a quench. For example, in the conserved case, where $L \sim t^{1/3}$, typical domain-wall speeds are $v \sim \dot{L} \sim t^{-2/3}$, and in the non-conserved case, where $L \sim t^{1/2}$, typical domain-wall speeds are $v \sim \dot{L} \sim t^{-1/2}$,

so a fixed time-step results in decreasing amounts of domain wall motion per step as time increases. This implies that the Euler update is very inefficient, and in practice it is computationally costly to use to evolve large systems until the late time scaling regime.

Various computational algorithms have been developed by increasing Δt compared to the simplest Euler discretization. For example, the Cell-Dynamical-Scheme (CDS) [20] exploits universality to choose a free energy that is convenient in terms of numerical stability, but then applies a fixed-step Euler algorithm to it. More recently, Fourier spectral methods [21, 22] have been developed by introducing implicit terms in the Fourier transform of the equation of motion (this is equivalent to $a_1 = 1$ and $a_2 = 0$ case in our unconditionally stable algorithms), and have been shown to allow an increase of the maximum time step Δt by two orders of magnitude. While CDS was broadly applied [23, 24], the Fourier spectral method was not. Neither of these two methods can adjust to the naturally slowing dynamics, so they eventually become more and more inefficient at the late time scaling regime.

2.2 Unconditionally stable algorithms

Before introducing the algorithms, it is interesting to know the nature time-step of the dynamics. The interface moves through a point in a time $\delta t \sim \xi/v \sim t^{2/3}$ in conserved systems and $\delta t \sim \xi/v \sim t^{1/2}$ in non-conserved systems, so the natural time step should also scale as

$$\Delta t_{CO} \sim t^{2/3}, \tag{2.4}$$

and

$$\Delta t_{NC} \sim t^{1/2} \tag{2.5}$$

in conserved and non-conserved systems, respectively.

Ideally, we want a numerical algorithm that efficiently integrates the CH and TDGL equations by moving the interface by a small fraction of the domain wall width at each time-step without encountering numerical instabilities. Unconditionally stable algorithms [25, 26, 27] are a class of stable algorithms free of the fixed time step

constraint for CH and TDGL dynamics due to a mix of implicit and explicit terms. A general family of such mixed algorithms for the TDGL equation in an arbitrary dimension is

$$\tilde{\phi}_{t+\Delta t} + (a_1 - 1)\Delta t\tilde{\phi}_{t+\Delta t} + (a_2 - 1)\Delta t\nabla^2\tilde{\phi}_{t+\Delta t} = \phi_t + \Delta t(a_1\phi_t + a_2\nabla^2\phi_t - \phi_t^3), \tag{2.6}$$

while for the CH equation, we have

$$\tilde{\phi}_{t+\Delta t} - (a_1 - 1)\Delta t\nabla^2\tilde{\phi}_{t+\Delta t} - (a_2 - 1)\Delta t\nabla^4\tilde{\phi}_{t+\Delta t} = \phi_t - \Delta t(a_1\nabla^2\phi_t + a_2\nabla^4\phi_t - \nabla^2\phi_t^3). \tag{2.7}$$

Implicit terms ($\tilde{\phi}_{t+\Delta t}$) are on the left and $\sim$ indicates that $\tilde{\phi}_{t+\Delta t}$ is not precisely obtained by the Cahn-Hilliard dynamics. The explicit terms (ϕ_t) are on the right. Eq.(2.6) and Eq.(2.7) are called "direct steps" since they can be directly solved for $\tilde{\phi}_{t+\Delta t}$ in Fourier space. When $a_1 = a_2 = 1$ these two equations correspond to the simple Euler update Eq.(2.1) and Eq.(2.2) without implicit terms.

In our simulations in conserved systems using the direct update, we use parameters $\Delta x = 1$, $a_1 = 3$ and $a_2 = 0$. The two dimensional order parameter is initially chosen to be randomly distributed between -1 and $+1$, and with periodic boundary conditions. The discretized Laplacian (see Appendix A) is generated by using both the nearest neighbor and the next nearest neighbor to reduce lattice anisotropy. In non-conserved systems, everything is the same except that we vary a_1 and a_2 to explore the Δt_s-dependence on them (see Chapter 4).

Chapter 3

Instabilities and Stabilities

Stability is crucial to computer simulations, so the criterion of stability constrains the parameters a_1 and a_2 in Eq.(2.6) and Eq.(2.7). The stability limits the Euler algorithm (see Appendix A for details) by imposing a maximal threshold for the time-step, above which the simulation becomes unstable. In the systems we are studying, the energy density plays an important role as a criterion of stability — after the quench, the energy is continuously decreased by dissipative dynamics Eq.(1.6) and Eq.(1.7), so any increase of the energy corresponds to a numerical instability. If increasing energies are never seen for an algorithm for any $\Delta t > 0$, we call the algorithm "gradient stable". We have also checked the system snapshots, structures and interfacial profiles and have not found any evidence of remaining instabilities in gradient stable algorithms.

Vollmayr-Lee and Rutenberg [27] have implemented a von Neumann (vN) stability analysis, which is a linear stability analysis, since any gradient stable algorithm must be linearly stable. They found that all of the von Neumann stable algorithms are also numerically gradient stable. Their work suggests that it is useful to impose von Neumann linear stability analysis to determine a broadly parameterized class of potential unconditionally stable semi-implicit algorithms, and then to numerically check the algorithms that will be implemented.

3.1 Spinodal condition of non-conserved dynamics

von Neumann stability is a linear stability analysis around a constant phase $\phi = c$. We analyze the exact dynamics for physical instabilities that we will want to preserve in our discretized dynamics. Taking

$$\phi(\mathbf{x}, t) \equiv c + \eta(\mathbf{x}, t), \tag{3.1}$$

where $\eta(\mathbf{x},t)$ is the deviation from the constant solution, we linearize the exact non-conserved dynamics Eq.(1.7) to get

$$\dot{\eta} = \nabla^2\eta + \eta - 3c^2\eta. \tag{3.2}$$

Fourier transform this to get

$$\dot{\eta_{\mathrm{k}}} = (\lambda_{\mathrm{k}} + 1 - 3c^2)\eta_{\mathrm{k}}, \tag{3.3}$$

where $\lambda_{\mathrm{k}} = -k^2$. The stability condition $|\eta_{\mathrm{k},t+\Delta t}| < |\eta_{\mathrm{k},t}|$ requires

$$\lambda_{\mathrm{k}} + 1 - 3c^2 < 0, \tag{3.4}$$

which demonstrates the spinodal instability for the exact dynamics that we want to preserve when we consider the stability of our discretized computational algorithms. Note that the same instability is seen in conserved dynamics [27].

3.2 von Neumann linear stability analysis

Vollmayr-Lee and Rutenberg [27] have employed unconditional von Neumann conditions for linear stability [28] to identify possibly gradient stable algorithms for conserved dynamics. Here, we present a similar analysis for non-conserved dynamics.

We linearize Eq.(2.6) using $\phi(\mathbf{x},t) \equiv c + \eta(\mathbf{x},t)$ and take its Fourier transform to get

$$\begin{aligned}[1 + \Delta t\{(a_1 - 1) + \lambda_{\mathrm{k}}(a_2 - 1)\}]\eta_{\mathrm{k},t+\Delta t} \\ = [1 + \Delta t\{a_1 + \lambda_{\mathrm{k}}a_2 - 3c^2\}]\eta_{\mathrm{k},t}.\end{aligned} \tag{3.5}$$

We write this as

$$[1 + \Delta t\mathcal{L}]\eta_{t+\Delta t} = [1 + \Delta t\mathcal{R}]\eta_t, \tag{3.6}$$

where

$$\mathcal{L} \equiv (a_1 - 1) + \lambda_{\mathrm{k}}(a_2 - 1), \tag{3.7}$$

$$\mathcal{R} \equiv a_1 + \lambda_{\mathrm{k}}a_2 - 3c^2. \tag{3.8}$$

Solving Eq.(3.5) for $\eta_{k,t+\Delta t}$, we see that $|\eta_{k,t+\Delta t}| < |\eta_{k,t}|$ if and only if

$$\frac{|1+\Delta t\mathcal{R}|}{|1+\Delta t\mathcal{L}|} < 1. \tag{3.9}$$

This is the von Neumann linear stability criterion, which forces η to decrease in magnitude as the system evolves. We have

$$\frac{1+\Delta t\mathcal{R}}{1+\Delta t\mathcal{L}} < 1, \tag{3.10}$$

and

$$\frac{1+\Delta t\mathcal{R}}{1+\Delta t\mathcal{L}} > -1. \tag{3.11}$$

The inequality (3.10) implies $\mathcal{R} < \mathcal{L}$ since $\Delta t > 0$ and $\mathcal{L} > 0$:

$$0 < \mathcal{L} - \mathcal{R} = -1 - \lambda_k + 3c^2, \tag{3.12}$$

which recovers the spinodal condition (3.4). The inequality (3.11) implies

$$\Delta t(\mathcal{L}+\mathcal{R}) > -2. \tag{3.13}$$

In order to solve for this inequality, we need to distinguish two cases, i.e. CASE I: $\mathcal{L}+\mathcal{R} > 0$ and CASE II: $\mathcal{L}+\mathcal{R} < 0$.

First considering CASE I ($\mathcal{L}+\mathcal{R} > 0$), we have

$$\Delta t > -\frac{2}{\mathcal{L}+\mathcal{R}}, \tag{3.14}$$

which implies that to keep the system stable, Δt can take any arbitrary positive values. The condition $\mathcal{L}+\mathcal{R} > 0$ gives

$$2a_1 - 1 - 3c^2 + \lambda_k(2a_2 - 1) > 0. \tag{3.15}$$

If we choose $a_2 < 1/2$, then since $\lambda_k < 0$ we get $2a_1 - 1 - 3c^2 > 0$ independent of our spatial discretization. So our stability condition on the inequality (3.15) are:

$$\begin{aligned} a_1 &> 2, \\ a_2 &< 1/2, \end{aligned} \tag{3.16}$$

where we impose $c \in [-1, 1]$. In our numerics, we use $a_1 = 3$ and $a_2 = 0$ throughout this thesis for conserved dynamics. Next, considering CASE II ($\mathcal{L}+\mathcal{R} < 0$), we have

$$\Delta t < -\frac{2}{\mathcal{L}+\mathcal{R}}, \tag{3.17}$$

which implies that to keep the system stable, Δt, like the checkerboard instability in the Euler algorithm, has a threshold. This is in fact the generalization of the Euler instability threshold. To better illustrate this threshold, we define Δt_{eff} as

$$\Delta t_{eff} \equiv \frac{\Delta t}{1 + \Delta t \mathcal{L}}. \tag{3.18}$$

To express Δt in terms of Δt_{eff}, we have

$$\Delta t = \frac{\Delta t_{eff}}{1 - \Delta t_{eff} \mathcal{L}}. \tag{3.19}$$

Substituting the expression for Δt in inequality (3.17), we get

$$\Delta t_{eff}(\mathcal{L} - \mathcal{R}) < 2. \tag{3.20}$$

Noting the stability condition $\mathcal{L} - \mathcal{R} > 0$, we have

$$\Delta t_{eff} < \frac{2}{\mathcal{L} - \mathcal{R}} = \frac{2}{2 - \lambda_{\mathbf{k}}}, \tag{3.21}$$

where $c^2 = 1$ is applied. This recovers the form of the stability condition for Euler update in non-conserved systems (inequality (A.12)). This analysis indicates that outside the unconditionally gradient stable region, we will have a maximal stable Δt given by inequality (3.17).

3.3 Numerical tests of stability

von Neumann stability analysis is a common test for numerical stability [27], however, it does not provide a decisive criterion since it does not explore nonlinear contributions. Eyre's theorem, by imposing a strict non-increase of the energy density in time [25, 26, 27], provides sufficient but not necessary conditions for gradient stability. Fig.3.1 shows the results of the numerical tests. We checked that a single step of the direct algorithm only decreases the energy for various time-steps in the range $\Delta t \in (0, 10^4]$. Larger time-steps than $\Delta t = 10^4$ are not explored to avoid roundoff errors. We have found that no linearly stable algorithm is numerically gradient unstable, therefore in all cases, the algorithms that are von Neumann stable appear to be gradient stable as well.

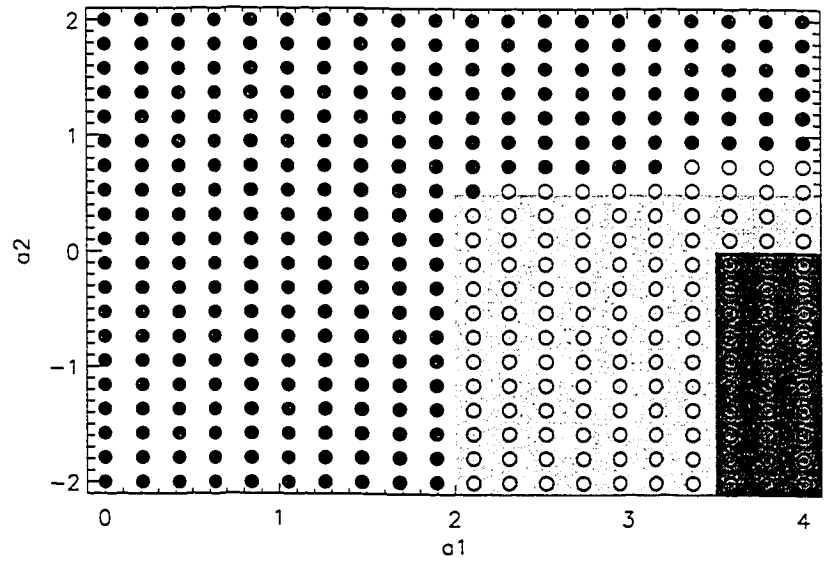

Figure 3.1: Numerically tested 400 direct algorithms Eq.(2.6) uniformly distributed with $a_1 \in [0,4]$, $a_2 \in [-2,2]$, for non-conserved systems, with system size of 512×512 and integrating forward to $t_{max} = 10^4$. We evolve systems with Euler updates ($\Delta t = 0.1$) and direct updates both with fixed $\Delta t = 100$ and with an increasing time-step $\Delta t = 0.1t^{1/4}$. The dark shaded region corresponds to Eyre stable algorithms (provably gradient stable), the light shaded corresponds to absolutely linear stable algorithms (von Neumann test), and the open circle denote algorithms that are numerically gradient stable under all of our tests. Any system that ever increased its free energy in a single update is labeled gradient unstable (filled circle). Inequality (3.15) implies that for a given $a_1 > 2$ and specific lattice $\lambda_{\mathbf{k}}$, we can have larger a_2. As a_1 is larger, we have more chance to have larger a_2. This is the reason we see some open circles outside the light shaded region. However we should note that (a_1,a_2) outside the stability bounds is lattice-dependent, so are risky to depend on. For most of the thesis, we use $a_1 = 3$ and $a_2 = 0$, which are gradient stable under numerical tests.

Chapter 4

Accuracy

With the unconditional stable algorithms described by Eq.(2.6) and Eq.(2.7), we will be able to take arbitrarily large time-steps. We now need to consider the accuracy of the algorithms. With the traditional Euler algorithm, accuracy is not an issue since the Euler algorithm becomes more and more accurate as time increases (see Chapter 6 for a detailed discussion). With the accelerated algorithms, we hope to control the error at an arbitrary but fixed level, so that we can trade unneeded accuracy for speed.

In principle, we can take $\Delta t \to \infty$, but we also want to keep track of the system evolution, so we need an independent measure of time rather than just $\sum \Delta t$. In this chapter, we introduce the Fourier-space effective time-step $\Delta t_{eff}(k, \Delta t)$ and the structural time-step Δt_s. These unconditionally stable algorithms act quite differently in conserved and non-conserved systems as revealed by the effective time-step and structural time-step. They provide a truly accelerated scheme in conserved systems, but only a fixed time-step scheme in non-conserved systems. These conclusions are supported by calculations for both conserved and non-conserved systems. Focusing on conserved systems, we discuss the single-step accuracy and the multi-step accuracy, which is a cumulative effect of the single-step error. We also discuss the accuracy of correlation functions in the scaling regime, which we measure numerically. Finally, by examining the accuracy of the multi-step error in the non-conserved systems, we find that unconditionally stable algorithms only give a small relative speedup compared to the arbitrarily accurate Euler algorithm.

4.1 Effective time-step

First we consider non-conserved systems. We re-express $\tilde{\phi}_{t+\Delta t}(\mathbf{x})$ and $\phi_t(\mathbf{x})$ on both sides of Eq.(2.6) by their Fourier Transform $\phi_{\mathbf{k}} \equiv \sum_{\mathbf{x}} e^{-i\mathbf{k}\cdot\mathbf{x}}\phi(\mathbf{x})$ and obtain

$$\begin{aligned} & \tilde{\phi}_{\mathbf{k},t+\Delta t} + (a_1 - 1)\Delta t\tilde{\phi}_{\mathbf{k},t+\Delta t} + (a_2 - 1)\Delta t\lambda_{\mathbf{k}}\tilde{\phi}_{\mathbf{k},t+\Delta t} \\ = \; & \phi_{\mathbf{k},t} + (a_1 - 1)\Delta t\phi_{\mathbf{k},t} + (a_2 - 1)\Delta t\lambda_{\mathbf{k}}\phi_{\mathbf{k},t} + \Delta t[\phi_{\mathbf{k},t} + \lambda_{\mathbf{k}}\phi_{\mathbf{k},t} - (\phi^3)_{\mathbf{k},t}], \quad (4.1) \end{aligned}$$

where the Fourier-transformed Laplacian $\lambda_{\mathbf{k}} = -k^2$. Therefore,

$$\tilde{\phi}_{\mathbf{k},t+\Delta t} = \phi_{\mathbf{k},t} + \frac{\Delta t[\phi_{\mathbf{k},t} + \lambda_{\mathbf{k}}\phi_{\mathbf{k},t} - (\phi^3)_{\mathbf{k},t}]}{1 + \Delta t[(a_1 - 1) + \lambda_{\mathbf{k}}(a_2 - 1)]} \quad (4.2)$$

$$= \phi_{\mathbf{k},t} + \frac{\Delta t\dot{\phi}_{\mathbf{k},t}}{1 + \Delta t[(a_1 - 1) + \lambda_{\mathbf{k}}(a_2 - 1)]} \quad (4.3)$$

Note that when $a_1 = a_2 = 1$, the above equation reduces to Euler update

$$\phi^{Eu}_{\mathbf{k},t+\Delta t} = \phi_{\mathbf{k},t} + \Delta t_{Eu}\dot{\phi}_{\mathbf{k},t}. \quad (4.4)$$

Comparing Eq.(4.3) with Eq.(4.4), we are led to define the effective time-step

$$\Delta t^{NC}_{eff}(k, \Delta t) \equiv \frac{\Delta t}{1 - \Delta t\hat{N}}, \quad (4.5)$$

where

$$\hat{N} = (1 - a_1) + (1 - a_2)\lambda_{\mathbf{k}}, \quad (4.6)$$

so we can rewrite Eq.(4.3) in a way analogous to Eq.(4.4)

$$\phi_{\mathbf{k},t+\Delta t} = \phi_{\mathbf{k},t} + \Delta t_{eff}\dot{\phi}_{\mathbf{k},t}. \quad (4.7)$$

Eq.(4.5) indicates that

$$\Delta t^{NC}_{eff}(k, \Delta t) \leq \Delta t^{NC}_{eff}(k, \infty) = \frac{1}{a_1 - 1 + k^2(1 - a_2)} < \frac{1}{a_1 - 1}, \quad (4.8)$$

where $a_1 - 1 > 0$ and $1 - a_2 > 0$ are used. Therefore, we cannot obtain an accelerated algorithm in non-conserved systems since there is an upper bound for the effective time-step $\Delta t^{NC}_{eff}(k, \Delta t)$.

In conserved systems, we can obtain the expression for Δt_{eff} in a similar way:

$$\Delta t_{eff}^{CO}(k, \Delta t) \equiv \frac{\Delta t}{1 - \Delta t \hat{K}}, \tag{4.9}$$

where

$$\hat{K} = (a_1 - 1)\lambda_{\mathbf{k}} + (a_2 - 1)\lambda_{\mathbf{k}}^2. \tag{4.10}$$

For an accurate algorithm, we require $\Delta t_{eff}^{CO}(1/L, \Delta t) \approx \Delta t$ since most structures are at $k \sim 1/L$. This condition yields $\Delta t \lesssim t_s^{2/3}$, allowing an accelerated algorithm $\Delta t = A t_s^{2/3}$. This is a truly accelerated algorithm since $\Delta t_{eff}^{CO}(k, \Delta t)$ grows with t_s. We see that $\Delta t_{eff}(k, \Delta t)$ is an effective time-step for a mode k, corresponding to an algorithmic time-step Δt. We shall confirm these tentative observations in the next several sections in this chapter.

4.2 Structural time-step in conserved systems

For both conserved and non-conserved scalar order parameters, we can calculate the scaling behavior of the energy density, E, which is expressed by the gradient term of Eq.(1.1) [30, 31]:

$$\begin{aligned} E &\sim \langle (\nabla \phi)^2 \rangle, & (4.11) \\ &\sim \int d^2k \;\; k^2 \langle \phi_{\mathbf{k}}(t) \phi_{-\mathbf{k}}(t) \rangle, & (4.12) \\ &= \int d^2k \;\; k^2 L^2 g(kL), & (4.13) \end{aligned}$$

where we restrict the calculation to two-dimensions, $d = 2$, for comparison with our numerical work (though it is easily generalized). As $kL \gg 1$,

$$g(kL) \sim \frac{1}{k^3 L^3}, \tag{4.14}$$

and we have

$$E \sim \int d^2k \frac{1}{kL} = \int k dk d\varphi \frac{1}{kL} \sim \int dk \frac{1}{L}. \tag{4.15}$$

Although theoretically the largest $k = \pi/\Delta x$, where Δx is the lattice spacing, the effective large-k cutoff is imposed by the interfacial structure, i.e. by the Porod tail

dropping away above $1/\xi$ (see Fig.4.2), where ξ is the domain wall width. Therefore,

$$E \sim \int_{1/L}^{1/\xi} dk \frac{1}{L} \sim \frac{1}{\xi L} \sim \frac{1}{t^{\alpha}}, \tag{4.16}$$

where $L(t) \sim t^{\alpha}$ [1] is used.

The k-dependent effective time-step Eq.(4.5) and Eq.(4.9) provide a measure of the system evolution in Fourier-space, however, it changes for each mode. The energy density E, on the other hand, serves a good probe for the system evolution, and easy to measure. This leads us to introduce an empirical "structural time" in terms of the monotonically decaying energy density E,

$$t_s \equiv \frac{B}{E^{1/\alpha}}, \tag{4.17}$$

where B is conveniently calibrated so that $\Delta t_s = \Delta t$ as $\Delta t \to 0$ in the late-time scaling regime, and $\alpha = 1/3$ or $1/2$ for conserved or non-conserved coarsening, respectively. The evolution of the structural time probes the real-world speed-up of our coarsening algorithms, and it also turns out to provide important insight into the observed errors of the scaled correlations. The relation between the structural time-step and the effective time-step in Fourier-space will be discussed in Chapter 6.

From Eq.(4.17), we have

$$E = \left(\frac{B_{CO}}{t_s} \right)^{1/3} \tag{4.18}$$

for conserved dynamics, and

$$\Delta t_s = \frac{-3 B_{CO} \Delta E}{E^4} = \frac{-3 \Delta E t_s^{4/3}}{B_{CO}^{1/3}}. \tag{4.19}$$

On the other hand, integrating E from each Fourier mode and using the Fourier transform of conserved dynamics Eq.(1.6):

$$\frac{\delta F}{\delta \phi_k} = -k^{-2} \dot{\phi}_{-k}, \tag{4.20}$$

we have

$$\Delta E \simeq \int_0^{1/\xi} d^2k \frac{1}{(2\pi)^2} \left\langle \left(\frac{\delta F}{\delta \phi_k} \right) \Delta \phi_k \right\rangle, \tag{4.21}$$

$$= -\int_0^{1/\xi} d^2k \frac{1}{(2\pi k)^2} \Delta t_{eff}^{CO}(k, \Delta t) T_k, \tag{4.22}$$

where the approximation in the first line is because the large-k cutoff is not exactly at $1/\xi$. The time-derivative correlation function

$$T_k \equiv \langle \dot{\phi}_k \dot{\phi}_{-k} \rangle \tag{4.23}$$

was used in the energy-scaling calculations [1, 30, 31], and has a natural scaling form given by

$$T_k = \dot{L}^2 h(kL) = \frac{L_0^2 h(kL)}{9 t_s^{4/3}}, \tag{4.24}$$

where $L = L_0 t_s^{1/3}$ and $h(x)$ is the scaling function. We can then solve for ΔE in Eq.(4.22) and thus for the structural time-step Δt_s from Eq.(4.19). Using Eq.(4.9), we have

$$\frac{\Delta t_s}{\Delta t} = C \int_0^{L/\xi} \frac{dx}{x} \frac{h(x)}{1 + \frac{\Delta t(a_1 - 1)}{L^2} x^2 + \frac{\Delta t(1 - a_2)}{L^4} x^4}, \tag{4.25}$$

$$= C \int_0^{L/\xi} \frac{dx}{x} \frac{h(x)}{1 + \frac{A(a_1 - 1)}{L_0^2} x^2 + \frac{A(1 - a_2)}{L_0^2 L^2} x^4}, \tag{4.26}$$

where $C = \dfrac{L_0^2}{6\pi B_{CO}^{1/3}}$, $x = kL$ and $\Delta t = A t_s^{2/3}$ is used, and ξ is proportional to the domain wall width. As $x \to L/\xi \to \infty$, the integrand is 0 because $h(x)$ is at most a constant at large x. For a fixed x, the x^4 term is negligible. So we do not have any a_2 dependence. We then obtain

$$\frac{\Delta t_s}{\Delta t} = C \int_0^{L/\xi} dx \frac{h(x)}{x + A' x^3} \equiv f(A'), \tag{4.27}$$

where

$$A' \equiv \frac{A(a_1 - 1)}{L_0^2}. \tag{4.28}$$

$\Delta t_s / \Delta t$ is t_s-independent in the scaling regime where $L = L_0 t_s^{1/3}$ applies since it is ultraviolet convergent. The form of $h(x)$ as $x \gg 1$ [31] (see Appendix E) is

$$h(x) = \frac{D}{x}, \tag{4.29}$$

where D is a prefactor. We split the integral into two pieces $(0, x_0)$ and $(x_0, L/\xi)$, where $x_0 \gg 1$ is a constant. Thus

$$f(A') = I_1(A') + I_2(A'), \tag{4.30}$$

where

$$I_1(A') = C \int_0^{x_0} \frac{dx}{x} \frac{h(x)}{1 + A'x^2}, \tag{4.31}$$

and

$$I_2(A') = CD \int_{x_0}^{L/\xi} \frac{dx}{x^2 + A'x^4}. \tag{4.32}$$

When $A' \to 0$, we obtain

$$I_1(0) = C \int_0^{x_0} \frac{h(x)}{x} dx, \tag{4.33}$$

and

$$I_2(0) = \frac{CD}{x_0} \tag{4.34}$$

when $L/\xi \to \infty$. From the definition of Δt_s, we should recover that $f(0) = 1$ because $\Delta t_s = \Delta t$.

Next we consider the case when $0 < A' \ll 1$. Expanding the right hand side of Eq.(4.31), we have

$$\begin{aligned} I_1(A') &= C \int_0^{x_0} \frac{h(x)}{x} dx - CA' \int_0^{x_0} h(x) x dx + O(A'^2), & (4.35) \\ &= I_1(0) + O(A'). & (4.36) \end{aligned}$$

Directly solving the integral on the right hand side of Eq.(4.32), we can get the explicit form for $I_2(A')$:

$$\begin{aligned} I_2(A') &= CD \left[-\sqrt{A'} \tan^{-1} \left(\frac{\sqrt{A'} L}{\xi} \right) - \frac{\xi}{L} + \sqrt{A'} \tan^{-1}(\sqrt{A'} x_0) + \frac{1}{x_0} \right], & (4.37) \\ &= CD \left[\frac{1}{x_0} - \frac{\pi}{2} \sqrt{A'} + \sqrt{A'} \tan^{-1}(\sqrt{A'} x_0) \right], & (4.38) \\ &= I_2(0) - \frac{\pi}{2} CD \sqrt{A'} + O(A'), & (4.39) \end{aligned}$$

where $L \to \infty$ at late times. Finally using Eq.(4.30), we obtain that, as A' is small,

$$1 - \frac{\Delta t_s}{\Delta t} = 1 - f(A') = \frac{\pi}{2} CD\sqrt{A'} + O(A'). \tag{4.40}$$

Eq.(4.40) implies that as $A' \to 0$, $1 - f(A') \to 0$. Also, $1 - f(A') = 0$ in the Euler algorithm in the $L/\xi \to \infty$ limit. The value of C can be obtained from the numerical data, and the value of the time-derivative correlation Porod-amplitude D has not been precisely measured. $1 - f(A') > 0$ for finite A' indicates that less energy is dissipated in a time-step than would be exactly integrated CH dynamics Eq.(1.6), and it can be related to the error in correlations. We will discuss $f(A')$ in more detail in the next section.

4.3 Accuracy in conserved systems

For conserved systems, the analysis in Section 4.2 indicates that we can use a time-step that is proportional to the natural time-step of conserved systems, $\Delta t = A t_s^{2/3}$ (see Fig.4.1 for a plot). With our unconditional stable algorithms Eq.(2.7), we can use such a progressively larger time-step as the dynamics slows at late times. However, the accuracy should be determined by the prefactor A. We can study the single-step error by obtaining an explicit expression of $\tilde{\phi}_{t+\Delta t}$ in terms of ϕ_t. We will then use these expressions to obtain a useful bound on the multi-step error.

At a given time t, we can formally expand $\tilde{\phi}_{t+\Delta t}$ in powers of Δt:

$$\tilde{\phi}_{t+\Delta t} = \phi_t + \sum_{n=1}^{\infty} \alpha_n \Delta t^n, \tag{4.41}$$

where α_n are independent of Δt. Substituting $\tilde{\phi}_{t+\Delta t}$ into Eq.(2.7), we have

$$\sum_{n=1}^{\infty} \alpha_n \Delta t^n + [(1-a_1)\nabla^2 \alpha_n + (1-a_2)\nabla^4 \alpha_n]\Delta t^{n+1} = -\Delta t \nabla^2 (\phi_t + \nabla^2 \phi_t - \phi_t^3). \tag{4.42}$$

The right hand side is just $\dot{\phi}_t \Delta t$. Comparing all the Δt^n terms on both sides, we have

$$\alpha_1 = \dot{\phi}_t, \tag{4.43}$$

$$\alpha_{n+1} = \hat{K}_r \alpha_n \quad (n \geq 1), \tag{4.44}$$

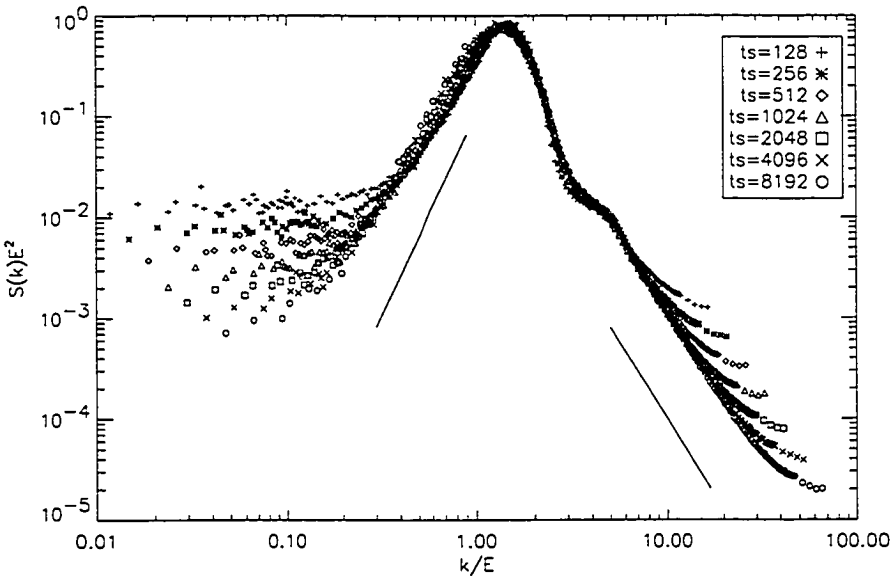

Figure 4.1: Plot of $S(k)E^2$ vs k/E in conserved systems, with Direct update, $\Delta t = 0.01t^{2/3}$, $L_{sys} = 2048$, averaged 20 samples. The two reference lines are $\sim x^4$ as k is small [46] and $\sim x^{-3}$, which is corresponding to the Porod tail [29]. In this plot, we see excellent scaling collapse at different structural time t_s in the scaling regime.

where

$$\hat{K}_r \equiv (a_1 - 1)\nabla^2 + (a_2 - 1)\nabla^4. \tag{4.45}$$

We obtain

$$\tilde{\phi}_{t+\Delta t} = \phi_t + \sum_{n=1}^{\infty} \Delta t^n \hat{K}_r^{n-1} \dot{\phi}. \tag{4.46}$$

The real-space single-step error is obtained by comparing with the exactly evolved field $\phi(t_s + \Delta t_s)$ that has the same energy:

$$\Delta\tilde{\phi}^s \equiv \tilde{\phi}(t_s + \Delta t) - \phi(t_s + \Delta t_s), \tag{4.47}$$

$$= \sum_{n=1}^{\infty} \Delta t^n \hat{K}_r^{n-1} \dot{\phi} - \sum_{n=1}^{\infty} \frac{\partial_t^n \phi}{n!} \Delta t_s^n, \tag{4.48}$$

where

$$\phi(t_s + \Delta t_s) = \phi(t_s) + \Delta t_s \partial_t \phi + \frac{1}{2}\Delta t_s^2 \partial_t^2 \phi + \frac{1}{3!}\Delta t_s^3 \partial_t^3 \phi + \ldots \tag{4.49}$$

is the Taylor expansion and $\tilde{\phi}(t_s + \Delta t)$ represents the field by the accelerated algorithm. Note that we compare the fields at the same energy, so we use Δt_s for the

exactly evolved field.

Since $\partial_t^n \phi \sim t_s^{-1/3-2n/3}$ and $(\nabla^2)^n \dot{\phi} \sim t_s^{-1-2n/3}$ in the bulk [27], if we take $\Delta t = At_s^{2/3}$ with small A, we can ignore the higher order terms $O(A^2)$ in the sum in Eq.(4.48), and we obtain

$$\Delta\tilde{\phi}^s = (\Delta t - \Delta t_s)\dot{\phi} + O(A^2)t_s^{-1/3}, \tag{4.50}$$

$$= (1 - F(A'))At_s^{-1/3} + O(A^2)t_s^{-1/3}, \tag{4.51}$$

$$\sim A^{3/2}t_s^{-1/3}. \tag{4.52}$$

A previous study [27] showed that these unconditionally stable algorithms do not allow a time-step $\Delta t \sim t^\beta$ with $\beta > 1/3$ because their single-step error in real-space near the interface would grow without bound. In Sec.III.A of [27], the scaling of the real-space error near interfaces at $O(\Delta t^n)$ for direct conserved algorithms should be $O(\dot{\phi}) \sim t^{-2/3}$ for all $n \geq 2$. Fig.4.2 indicates that the interface profile is properly maintained and the errors near the interface can be ignored. Therefore, we should only consider the errors in the bulk.

Next we consider the multi-step error. At worst this single-step error will accumulate with each update. Evolving to t_s with time-step $\Delta t = At_s^{2/3} \sim dt_s/dn$ requires the number of steps

$$n = \int_0^{t_s} \frac{dt_s}{At_s^{2/3}} = \frac{3t_s^{1/3}}{A} \sim \frac{L(t_s)}{A}. \tag{4.53}$$

So we place an upper bound on the multi-step error for system evolving from the beginning to t_s as

$$\Delta\tilde{\phi}^m \sim \Delta\tilde{\phi}^s n \sim A^{3/2}t_s^{-1/3}\frac{L(t_s)}{A} \sim \sqrt{A}. \tag{4.54}$$

If we consider the error for the real-space correlation function $f(r/L) = \langle\phi(x)\phi(x+r)\rangle$, we obtain $\Delta f \simeq 2\Delta\tilde{\phi}_k^m\phi \sim \sqrt{A}$.

Besides considering the error spatially; i.e. at a given position, we can also consider the error at a particular k-value or mode. The Fourier space single-step error is, using Eq.(4.7) and Eq.(4.9),

$$\Delta\tilde{\phi}_k^s \equiv \tilde{\phi}_k(t_s + \Delta t) - \phi_k(t_s + \Delta t_s), \tag{4.55}$$

$$= \frac{\Delta t\dot{\phi}_k}{1 - \Delta t\hat{K}} - \sum_{n=1}^{\infty}\frac{\partial_t^n\phi_k}{n!}\Delta t_s^n, \tag{4.56}$$

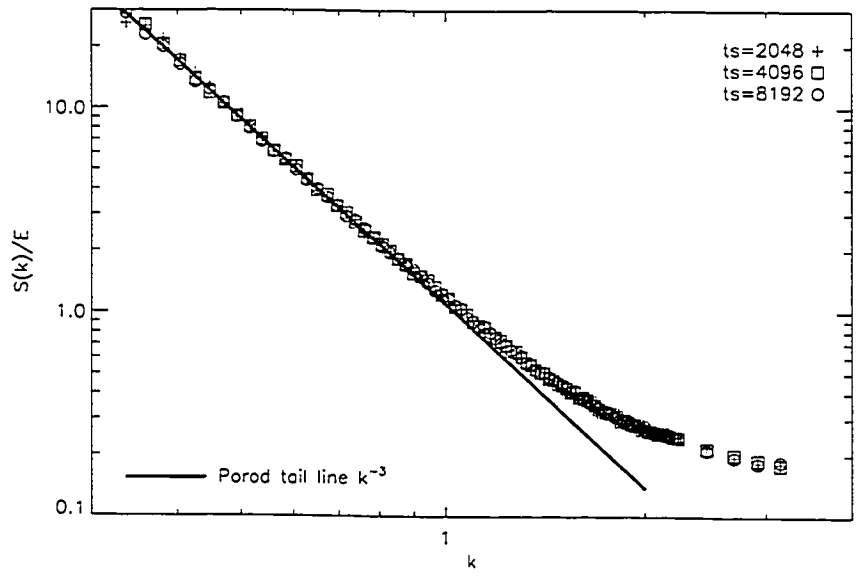

Figure 4.2: A plot of $S(k)/E$ vs k to show the interfacial profile in conserved systems, $L_{sys} = 2048$, driven by $\Delta t = 0.01 t_s^{2/3}$, averaged over 20 samples. The Porod tail [29] line of k^{-3} represents $S(k)/E$ in the sharp interface limit. The data that deviated from the Porod tail line (thick solid line) reflects the interfacial profile at $k \sim 1/\xi$, where ξ is the domain wall width. We compare the interfacial profiles for three different t_s in the scaling regime, and see that the domain wall profile does not change with respect to time. Note $k_{max} = \pi/\Delta x = \pi$.

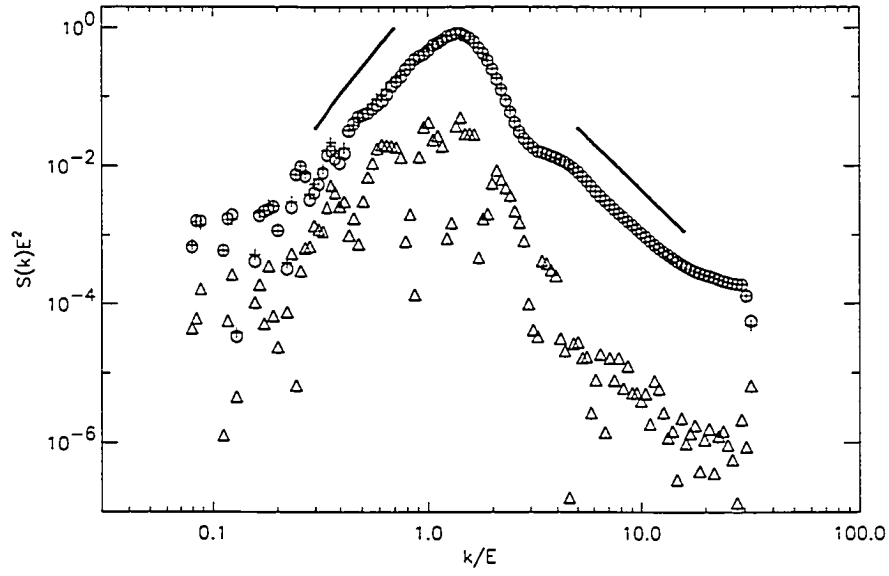

Figure 4.3: Plot of $S(k)E^2$ vs k/E for $L_{sys} = 512$ at $t_s = 1024$ with the Euler update (circles) with $\Delta t = 0.03$ and the Direct update ("+") with $\Delta t = 0.01 t_s^{2/3}$. We see excellent overlap between these computational algorithms. Triangles indicate the absolute difference between Direct and Euler updates. To quantify the error at a certain t_s, we take the absolute value of the maximal value of the difference between the scaled structures. We find that this maximum difference is approximately constant in magnitude throughout the late time scaling regime. See Fig.4.4 for a summary of errors of different A.

where $\phi_k(t_s+\Delta t_s)$ is the exactly evolved field, and $\hat{K} = -(a_1-1)k^2-(1-a_2)k^4 \leq 0$. For small values of the prefactor A, using $|\partial_t^n \phi_k| \sim t_s^{-2n/3-1/6}$ as $n > 1$ (see Eq.(E.11)), the $n \geq 2$ terms are $O(A^2)$ and sub-dominant (see below). The Fourier-space single-step error becomes

$$\Delta\tilde{\phi}_k^s \simeq \frac{\Delta t\dot{\phi}_k}{1+\Delta t k^2(a_1-1)} - \Delta t_s\dot{\phi}_k, \tag{4.57}$$

$$= \frac{-\Delta t\Delta t_s\dot{\phi}_k k^2(a_1-1)+(\Delta t-\Delta t_s)\dot{\phi}_k}{1+\Delta t k^2(a_1-1)}, \tag{4.58}$$

$$\sim \frac{[-A'f(A')x^2+1-f(A')]A\sqrt{h(x)}}{1+x^2A'}, \tag{4.59}$$

where $A' = \frac{A(a_1-1)}{L_0^2}$, $f(A') \equiv \frac{\Delta t_s}{\Delta t}$, $x \equiv kL$, $L = L_0 t_s^{2/3}$ and $\dot{\phi}_k \sim t_s^{-2/3}$ (see Eq.(E.11)) are used. We find numerically that the single-step error is largest at $x \approx 1$ (data not shown), and this is reasonable since most of the structure is there. For small A, $1-f(A') \sim \sqrt{A'} \sim \sqrt{A}$, and using $x = O(1)$ and $h(x) = O(1)$, we find

$$\Delta\tilde{\phi}_k^s \lesssim \frac{A^{3/2}}{1+A'} + O(A^2). \tag{4.60}$$

Using Eq.(4.53), we obtain the upper bound on the multi-step error at t_s is

$$\Delta\tilde{\phi}_k^m \sim \Delta\tilde{\phi}_k^s n \lesssim \frac{A^{3/2}L(t_s)}{A} \sim L(t_s)\sqrt{A}. \tag{4.61}$$

We can use this to bound the error of the scaled correlation.

$$g(kL) = \frac{\langle|\phi_k|^2\rangle}{L^2(t_s)}, \tag{4.62}$$

which implies

$$\Delta g \simeq 2\frac{\Delta\tilde{\phi}_k^m\phi_k}{L^2} \sim \sqrt{A}. \tag{4.63}$$

It is interesting that the accumulated error in the correlations has the same form as $1-\Delta t_s/\Delta t$ in Eq.(4.40).

It is noted that our analysis are consistent in both Fourier-space and real-space. For a single update, the relative error is of the order $t_s^{-1/3}A^{3/2}$ as A is small — this guarantees that the relative error is bounded by $\sqrt{A}$ for multi-steps. Therefore, the

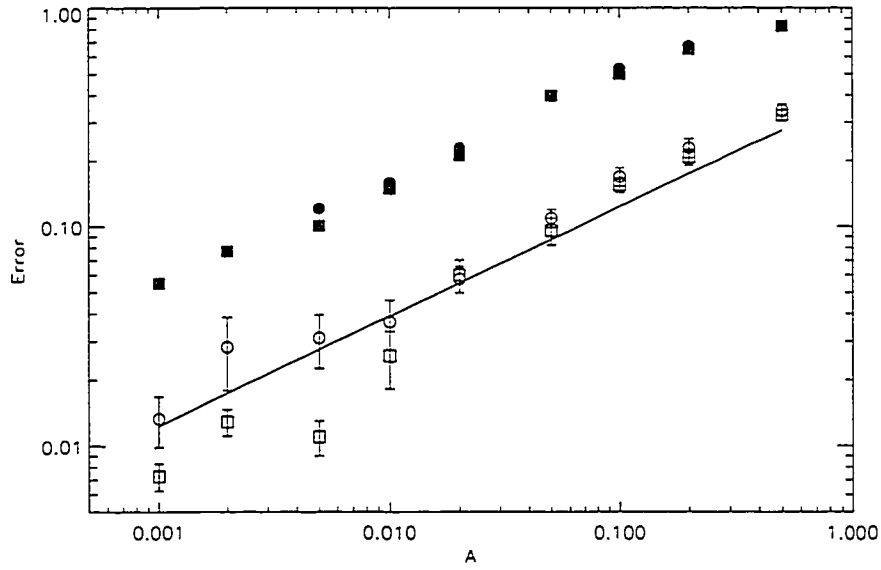

Figure 4.4: Plot of maximal difference of scaled structural factor vs A. The difference is obtained by comparison of scaled structural factor for conserved systems with Direct update ($\Delta t = A t_s^{2/3}$) with Euler update $\Delta t = 0.03$, and averaged in the scaling regime. The system sizes are $L_{sys} = 256$ (at least 200 samples, open square, averaged over 4 times in $t_s \in [60, 200]$) and $L_{sys} = 512$ (at least 20 samples, open circle, averaged over 9 times in $t_s \in [60, 1600]$). The error bars are obtained as variances by averaging in the scaling regime. For comparison, we also include the plot of time-step error $1 - \Delta t_s/\Delta t$ vs A. The system sizes are $L_{sys} = 256$ (at least 200 samples, filled square) and $L_{sys} = 512$ (at least 20 samples, filled circle). The reference line is $\sim \sqrt{A}$. We see that $1 - \Delta t_s/\Delta t \propto \sqrt{A}$, as predicted in Eq.(4.40), and $\Delta g \sim \sqrt{A}$, which confirms Eq.(4.63).

error compared with exact dynamics in both $g(kL)$ and $f(r/L)$ scales as $\sqrt{A}$ for small A.

In order to test accuracy, we quantitatively compare the accelerated algorithm with the standard fixed time-step Euler algorithm, which is a slow but accurate algorithm. We compare the scaled correlation function in the scaling regime to show the maximal difference between them is always around the peak and is time-independent. Thus we plot the averaged maximal difference in the scaling regime vs A and find that $\Delta \sim \sqrt{A}$ (see Fig.4.4).

The numerical result that we saturate the upper bound of the multi-step error indicates that the single-step error does not grow but accumulate over time. At the early time transient period, where all the order parameters start to choose either of the two equilibrium states to lower their energy, we do not expect the error to grow since that tends to increase energy. In the late time scaling regime, any error introduced in the bulk tends to decay to lower the energy. The error near the interface tends to decay too to maintain a fixed interfacial profile (see Fig.4.2). On the other hand, the error introduced in the interfacial motion tends to grow over time and becomes a cumulative effect. So these explains what we observe in Fig.4.4.

4.4 Structural time-step in non-conserved systems

In non-conserved systems, using Eq.(4.17) with $\alpha = 1/2$, we have

$$E = \left(\frac{B_{NC}}{t_s}\right)^{1/2}, \tag{4.64}$$

where B_{NC} is analogous to B_{CO} in conserved systems, and used to distinguish between non-conserved and conserved systems. From Eq.(4.17), we have

$$\Delta t_s = \frac{-2B_{NC}\Delta E}{E^3} = \frac{-2\Delta E t_s^{3/2}}{B_{NC}^{1/2}}. \tag{4.65}$$

Integrating E from each Fourier mode and using the Fourier transform of the non-conserved dynamics Eq.(1.7):

$$\frac{\delta F}{\delta \phi_k} = -\dot{\phi}_{-k}, \tag{4.66}$$

we have

$$\Delta E \simeq \int_0^{1/\xi} d^2k \frac{1}{(2\pi)^2} \left\langle \left(\frac{\delta F}{\delta \phi_k} \right) \Delta\phi_k \right\rangle, \tag{4.67}$$

$$= -\int_0^{1/\xi} d^2k \frac{1}{(2\pi)^2} \Delta t_{eff}^{NC}(k, \Delta t) T_k, \tag{4.68}$$

where the time-derivative correlation function T_k [1, 30, 31] has a natural scaling form of

$$T_k \equiv \langle \dot{\phi}_k \dot{\phi}_{-k} \rangle = \dot{L}^2 h(kL) = \frac{L_0^2 h(kL)}{4t_s}, \tag{4.69}$$

where $L = L_0 t_s^{1/2}$ and $h(x)$ is the scaling function. We can then solve for ΔE in Eq.(4.68) and for Δt_s from Eq.(4.65). Using Eq.(4.5), we have

$$\Delta t_s = C' \int_0^{1/\xi} \frac{kh(kL)\Delta t dk}{1 + \Delta t(a_1 - 1) + \Delta t k^2 (1 - a_2)}, \tag{4.70}$$

$$= C' \int_0^{L/\xi} \frac{xh(x)\Delta t dx}{[1 + \Delta t(a_1 - 1)]L^2 + \Delta t x^2 (1 - a_2)}, \tag{4.71}$$

$$= C' \int_0^{L/\xi} \frac{xh(x)\Delta t dx}{EL^2 + Fx^2}, \tag{4.72}$$

$$= C' \int_0^{x_0} \frac{xh(x)\Delta t dx}{EL^2 + Fx^2} + C'D' \int_{x_0}^{L/\xi} \frac{\Delta t dx}{EL^2 + Fx^2}, \tag{4.73}$$

$$= J_1 + J_2, \tag{4.74}$$

where $C' = \dfrac{L_0 L}{4\pi B_{NC}^{1/2}}$, $x = kL$, $E = 1 + \Delta t(a_1 - 1)$, $F = \Delta t(1 - a_2)$, ξ is the domain wall width and

$$J_1 = C' \int_0^{x_0} \frac{xh(x)\Delta t dx}{EL^2 + Fx^2} \tag{4.75}$$

and

$$J_2 = C'D' \int_{x_0}^{L/\xi} \frac{\Delta t dx}{EL^2 + Fx^2} \tag{4.76}$$

and

$$h(x) = \frac{D'}{x} \tag{4.77}$$

as $x = x_0 \gg 1$ is used. Now consider the integral J_1 as $0 \leq x \leq x_0$. We have $E \sim F \sim \Delta t$ for large Δt, and $E \sim 1$ and $F \sim \Delta t$ for small Δt, but $L^2 \to \infty$ at late

times — this implies that the denominator is infinite at late times for any Δt. Also since $h(x)$ is finite, $J_1 \to 0$ at late times. Therefore we have

$$\Delta t_s = J_2 = \Delta t \frac{C'D'}{L\sqrt{EF}} \left[\tan^{-1}\left(\sqrt{\frac{F}{E}}\frac{1}{\xi}\right) - \tan^{-1}\left(\sqrt{\frac{F}{E}}\frac{x_0}{L}\right)\right], \quad (4.78)$$

$$= \Delta t \frac{C'D'}{L\sqrt{EF}} \tan^{-1}\left(\sqrt{\frac{F}{E}}\frac{1}{\xi}\right), \quad (4.79)$$

where $L \to \infty$ is used in the late time scaling regime. With the condition $\Delta t_s = \Delta t$ as $\Delta t \to 0$, we obtain that

$$\xi = \frac{C'D'}{L}. \quad (4.80)$$

So we have

$$\Delta t_s = \frac{\Delta t \xi}{\sqrt{[1+\Delta t(a_1-1)]\Delta t(1-a_2)}} \tan^{-1}\left(\sqrt{\frac{\Delta t(1-a_2)}{1+\Delta t(a_1-1)}}\frac{1}{\xi}\right). \quad (4.81)$$

As $\Delta t \to \infty$, we obtain the maximal structural time-step:

$$\Delta t_s^{max} = \frac{\xi}{\sqrt{(a_1-1)(1-a_2)}} \tan^{-1}\left(\sqrt{\frac{1-a_2}{a_1-1}}\frac{1}{\xi}\right), \quad (4.82)$$

where ξ is an undetermined inverse ultraviolet cut-off expected to be close to the interfacial width. Eq.(4.82) implies

$$\Delta t_s^{max} < \frac{\xi}{\sqrt{(a_1-1)(1-a_2)}} \sqrt{\frac{1-a_2}{a_1-1}}\frac{1}{\xi} = \frac{1}{a_1-1}, \quad (4.83)$$

because $\tan^{-1}(x) < x$ for $x > 0$.

Unlike the conserved dynamics, in non-conserved dynamics, Δt_s can only have a finite value even if we drive $\Delta t \to \infty$. This is consistent with the early analysis of the effective time-step inequality (4.8). If we choose $a_1 = 2^+$ and $a_2 = 0.5^-$, we get $\Delta t_s^{max} \approx 0.84$, which is about 4 times the maximal time-step of Euler algorithm $\Delta t_{Eu} \approx 0.23$ for lattice spacing $\Delta x = 1$. In Fig.4.6, we show numerical results of Δt_s^{max} for various a_1 and a_2 to test Eq.(4.82) and some relevant discussion.

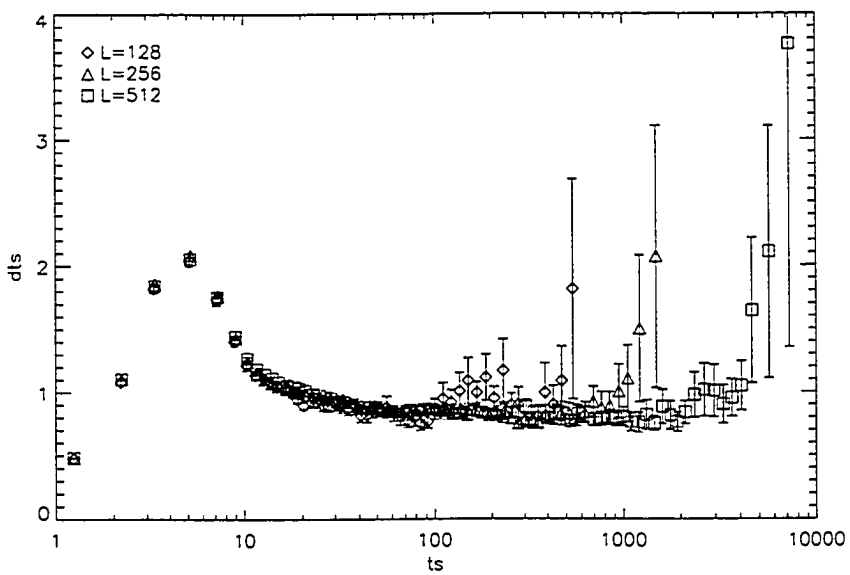

Figure 4.5: Plot of Δt_s^{max} vs t_s in non-conserved systems, with Direct update, $\Delta t \to \infty$, $a_1 = 2$ and $a_2 = 0.5$, averaged over 20 samples for each systems size. We see that $\Delta t_s^{max} \approx 0.84$ at late times. $L_{sys} = 128$, 256 and 512. This plot confirms a fixed structural time-step Δt_s^{max} in the scaling regime (see Eq.(4.82)). Also see a summary of Δt_s^{max} using various a_1 and a_2 in Fig.4.6.

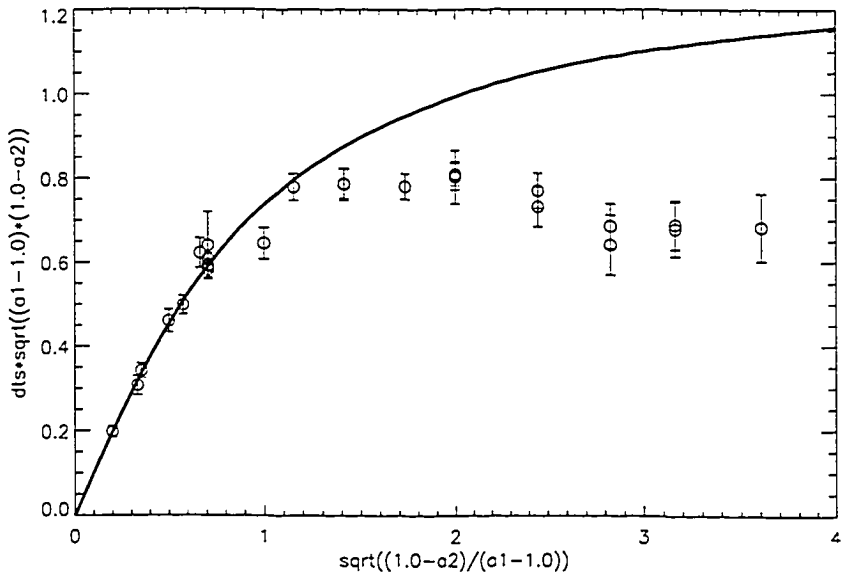

Figure 4.6: Plot of $\Delta t_s^{max}\sqrt{(a_1-1)(1-a_2)}$ vs $\sqrt{(1-a_2)/(a_1-1)}$ in non-conserved systems, with Direct update, $\Delta t \to \infty$, $L_{sys} = 512$, averaged 20 samples for various a_1 and a_2. The open circles denotes measured values. The error bars are obtained as variances by averaging over Δt_s^{max} in the scaling regime $t_s \in [100, 1000]$. The solid line denotes the theoretical prediction $y = \xi \tan^{-1}(x/\xi)$, where $\xi = 0.85$ for best fit. For small x, the fit is good, but for larger x, Eq.(4.82) is inconsistent with our measured Δt_s^{max}. The reasons for the inconsistency is that the systematic errors in time-derivative correlation function $T(k)$ become large as $\sqrt{(1-a_2)/(a_1-1)}$ is large [32] (the Fourier-space multi-step relative error increases monotonically with $\sqrt{(1-a_2)/(a_1-1)}$, see Section 4.5 for details).

4.5 Accuracy in non-conserved systems

For non-conserved systems, we do not get a truly accelerated algorithm since these unconditional stable algorithms allow us to drive $\Delta t \to \infty$, but we can only get a fixed structural time-step Δt_s and have a fixed speedup. In this section, we study the accuracy of this algorithm.

The Fourier space single-step error is

$$\begin{aligned} \Delta\tilde{\phi}_k &\equiv \tilde{\phi}_k(t_s+\Delta t) - \phi_k(t_s+\Delta t_s), && (4.84)\\ &= \frac{\Delta t\dot{\phi}_k}{1-\Delta t\hat{N}} - \sum_{n=1}^{\infty}\frac{\partial_t^n\phi_k}{n!}\Delta t_s^n, && (4.85)\end{aligned}$$

where $\phi_k(t_s+\Delta t_s)$ is the exactly evolved field, and $\hat{N} = -(a_1-1)-(1-a_2)k^2 \le 0$. Since $|\partial_t^n\phi_k| \sim t_s^{-n/2-1/4}$ as $n > 1$ (see Eq.(E.12)), and Δt_s is a constant, we can ignore the higher order terms of Δt_s in the sum. As $\Delta t \to \infty$, we obtain the Fourier space single-step error

$$\begin{aligned} \Delta\tilde{\phi}_k^s &= \frac{\dot{\phi}_k}{a_1 - 1 + k^2(1-a_2)} - \Delta t_s^{max}\dot{\phi}_k, && (4.86)\\ &\simeq \left[\frac{1}{a_1-1} - \Delta t_s^{max}\right]\dot{\phi}_k. && (4.87)\end{aligned}$$

Note the field scaling $\phi_k \sim L \sim t_s^{1/2}$ and $\dot{\phi}_k \sim \dot{L} \sim t_s^{-1/2}$ (see Eq.(E.12)) in non-conserved systems. Evolving to t_s with a fixed structural time-step Δt_s^{max} requires the number of steps $t_s/\Delta t_s^{max}$, so the Fourier-space multi-step relative error is at most

$$\begin{aligned} \frac{\Delta\tilde{\phi}_k^m}{\phi_k} &\le \left[\frac{1}{a_1-1} - \Delta t_s^{max}\right]\frac{\dot{\phi}_k t_s}{\phi_k \Delta t_s^{max}}, && (4.88)\\ &\sim \frac{1}{(a_1-1)\Delta t_s^{max}} - 1, && (4.89)\\ &= \frac{\sqrt{1-a_2}}{\xi\sqrt{a_1-1}\tan^{-1}\left(\sqrt{\frac{1-a_2}{a_1-1}}\frac{1}{\xi}\right)} - 1, && (4.90)\\ &= \frac{z}{\tan^{-1}(z)} - 1, && (4.91)\\ &= f(z), && (4.92)\end{aligned}$$

where $z \equiv \sqrt{\frac{1-a_2}{a_1-1}}\frac{1}{\xi}$. The function $f(z)$ monotonically increases with z. This indicates that the multi-step error upper bound increases with z. Numerically while

we do not observe a significant z-dependent error in the correlations, we observe a larger error in the time-derivative correlations as z is larger (data not shown), which leads the worse fitting as z is larger (see Fig.4.6). Surprisingly, although this algorithm Eq.(2.6) leads to a fixed structural time-step, the error does not approach 0 at late times as in the Euler algorithm with fixed time-step.

It is interesting to consider the relative speedup of these algorithms with respect to the standard Euler algorithm with a fixed time-step $\Delta t_{Eu} \approx 0.23$. The computer time per step for the direct update Eq.(2.6) is about 2.5 times the computer time per step for Euler update Eq.(2.1) because of the FFT needed for the direct update. Therefore we need $\Delta t_s^{max} > 0.23 \times 2.5 = 0.58$ to make this algorithm useful. Since $\Delta t_s^{max} < 1/(a_1 - 1)$ (see Eq.(4.83)), we need $a_1 < 1 + 1/0.58 = 2.74$. With $a_1 = 2.74$, we need $a_2 \to 0.5^-$ to obtain a minimal relative error bound $\Delta\tilde{\phi}_k/\phi_k \sim f(z) = 0.184$. With a non-zero error and small relative speedup (maximally $0.84/0.58 = 1.45$), we conclude that these algorithms in non-conserved systems, have no advantage over the arbitrarily accurate Euler algorithm.

Chapter 5

Universality classes of correlations

In phase ordering dynamics, there are universality classes of the non-equilibrium dynamical growth exponent α, where the characteristic length grow as $L(t) \sim t^{\alpha}$ at late times. In these universality classes, only conservation laws (non-conserved dynamics or conserved dynamics [16]), spatial dimensionality d and the order parameter dimensionality n are the parameters that affect the scaling exponents. The universality classes of the growth exponents were demonstrated by Renormalization Group (RG) methods [11] and the energy scaling method [30, 31].

Correlations of coarsening systems are important probes of their structure, and the characteristic length $L(t)$ is only part of the correlations. There has been little work on the universality classes of correlations. We think it is useful to understand the correlations and study universality class in correlations — which parameters affect the correlation, and which do not? The order parameter correlations in the coarsening systems have been found to depend on spatial dimensionality d and order parameter dimensionality n, even for systems with the same growth exponents [1]. For a given system, no dependence of correlations on the microscopic details of the numerical algorithm are expected. This underlies the usefulness of CH equation and other simplified dynamical models of coarsening phenomenon.

In this chapter, as an application of our accelerated algorithms, we explore the universality classes of correlations in conserved systems that result from introducing asymmetric bulk mobilities (Section 5.1). We also derive accelerated algorithms for the study of how anisotropic surface tension (Section 5.2) affect spatial correlations.

5.1 Asymmetric bulk mobilities

Eq.(1.6) describes conserved dynamics with a constant mobility $M_0 = 1$ and a symmetric double-well potential $V(\phi)$. A more general form will include an asymmetric

order-parameter-dependent bulk mobility $M(\phi)$ and an asymmetric potential $V(\phi)$. The general equations of motion are

$$\begin{aligned} \frac{\partial \phi}{\partial t} &= -\nabla \cdot \mathbf{j}, \\ \mathbf{j} &= -M(\phi)\nabla\mu, \\ \mu &= \frac{\delta F}{\delta \phi} = -\nabla^2\phi + V'(\phi), \end{aligned} \tag{5.1}$$

where $V'(\phi) = dV/d\phi$.

Following Bray [1], the Gibbs-Thomson boundary condition for a stationary interface gives the relation

$$\mu\Delta\phi = \Delta V - \sigma K \tag{5.2}$$

at the interface, where $\Delta\phi$ is the change in ϕ across the interface, ΔV is the difference in the minima of the potential for the two bulk phases and K is the curvature. Simplifying to the case where the minima have equal depth and taking the minima to be at $\phi = \pm 1$ as usual give $\Delta V = 0$ and $\Delta\phi = 2$. Then the above equation becomes

$$\mu = -\frac{\sigma K}{2}. \tag{5.3}$$

This condition determines μ on the interface in terms of the interfacial curvature.

Now consider the case of a single spherical domain of negative phase ($\phi = -1$) in an infinite sea of positive phase ($\phi = +1$) with asymmetric bulk mobilities $M_\pm \equiv M(\phi_\pm)$. Deep in the bulk, the chemical potential μ obeys the equation

$$\nabla^2\mu = 0. \tag{5.4}$$

Eq.(5.4) implies $\mu = 0$ at infinity. Let the domain have radius $R(t)$, and we have $K = 1/R$ in two dimensions. The solution of Eq.(5.4) that obeys the boundary conditions $\mu = 0$ at infinity and Eq.(5.3) at $r = R$ is

$$\mu = \begin{cases} -\dfrac{\sigma}{2R}, & r \le R \\ -\dfrac{\sigma}{2r}. & r \ge R \end{cases} \tag{5.5}$$

An interface moves with a velocity given by the imbalance between the current flowing into and out it:

$$v\Delta\phi = j_{out} - j_{in} = -M_+ \frac{\partial\mu}{\partial g}\bigg|_+ + M_- \frac{\partial\mu}{\partial g}\bigg|_-, \tag{5.6}$$

where ν is the speed of the interface in the direction of increasing ϕ. With $\Delta\phi = 2$, we have

$$\frac{dR}{dt} = \nu = -\frac{1}{2}\left(M_+ \frac{\partial\mu}{\partial r}\Big|_+ - M_- \frac{\partial\mu}{\partial r}\Big|_-\right) = -\frac{\sigma M_+}{4R^2}. \tag{5.7}$$

We see that the single spherical domain of $\phi = -1$ evaporates by the diffusion of negative phase to infinity, the rate of which is controlled by the bulk mobility M_+. Likewise, the evaporation of a single spherical domain of $\phi = +1$ is controlled by the bulk mobility M_-. This result shows that the process of coarsening is dominated by the bulk mobilities [1, 34], so we do not expect correlations to depend on the interfacial mobilities. Indeed, a study [18] of a conserved scalar system in two-dimensional with a symmetric order-parameter-dependent mobility which only changes in the interface showed that an interfacially varying but symmetric mobility does not change the spatial correlations unless it vanishes in the bulk phases. Some studies of asymmetric order-parameter-dependent mobility [17, 33] showed that the correlations change at early times. Because the bulk mobilities explicitly appear in the equation of motion Eq.(5.1), we expect the correlations of coarsening systems with asymmetric bulk mobilities are different from that with symmetric bulk mobilities. We can characterize asymmetric bulk mobilities by the dimensionless ratio

$$R \equiv \frac{M_-}{M_+} = \frac{M(\phi_-)}{M(\phi_+)}. \tag{5.8}$$

Note that $R = 1$ for symmetric phases where $M(\phi_+) = M(\phi_-)$.

We will introduce asymmetric mobility $M(\phi)$ and test whether correlations depend on R ($R \neq 1$).

5.1.1 Algorithms with asymmetric bulk mobilities

The simplest analytic method of implementing asymmetric mobilities in the bulk phase is through a linear mobility term

$$M(\phi) = 1 + a\phi, \tag{5.9}$$

where $a \in [0, 1]$. When $a = 0$, we recover the well-studied symmetric case. $V(\phi)$ is still the symmetric double-well form $V(\phi) = (\phi^2-1)^2/4$, which yields $\mu = -\nabla^2\phi + V'(\phi) =$

$-\nabla^2\phi - \phi + \phi^3$. Using Eq.(5.1), we obtain the equation of motion

$$\begin{aligned}\frac{\partial\phi}{\partial t} &= -\nabla\cdot[-(1+a\phi)\nabla\mu], \\ &= \nabla^2\mu + a\nabla\cdot[\phi\nabla\mu], \\ &= \nabla^2\mu + a\phi\nabla^2\mu + a\nabla\phi\cdot\nabla\mu. \end{aligned} \tag{5.10}$$

The bulk phases are at $\phi_\pm = \pm 1$. Therefore, the bulk mobilities are

$$M_\pm = M(\phi_\pm) = 1 \pm a, \tag{5.11}$$

and

$$R = \frac{1-a}{1+a}, \tag{5.12}$$

with $R \in [0,1]$ for $a \in [0,1]$.

To implement Eq.(5.10) with an unconditionally stable algorithm with direct parameterization, we introduce some implicit terms. Note that the choices of introducing implicit terms are not unique. Although different choices might lead to different constraints of the parameters, they all provide unconditionally stable algorithms. For simplicity, we use the same parameterization as used in Eq.(2.7):

$$\begin{aligned} & \tilde{\phi}_{t+\Delta t} + \Delta t\nabla^2[(1-a_1)\tilde{\phi}_{t+\Delta t} + (1-a_2)\nabla^2\tilde{\phi}_{t+\Delta t}] \\ = \;& \phi_t + \Delta t\nabla^2(-a_1\phi_t - a_2\nabla^2\phi_t + \phi_t^3) \\ + \;& a\Delta t\phi_t\nabla^2(-\phi_t - \nabla^2\phi_t + \phi_t^3) + a\Delta t\nabla\phi_t\cdot\nabla(-\phi_t - \nabla^2\phi_t + \phi_t^3). \end{aligned} \tag{5.13}$$

We do a von Neumann stability analysis of this equation, following the analysis of Section 3.2 and obtain the conditions for a_1 and a_2. Linearizing this equation around $\phi(\mathbf{x},t) \equiv c + \eta(\mathbf{x},t)$, where $\phi = c$ is a constant phase, and taking its Fourier Transform, we obtain

$$\begin{aligned} & [1 - \Delta t\lambda_{\mathbf{k}}\{(a_1-1) - \lambda_{\mathbf{k}}(1-a_2)\}]\eta_{\mathbf{k},t+\Delta t} \\ = \;& [1 - \Delta t\lambda_{\mathbf{k}}\{(a_1 + \lambda_{\mathbf{k}}a_2 - 3c^2) - (ac+a)(-1-\lambda_{\mathbf{k}} + 3c^2)\}]\eta_{\mathbf{k},t}. \end{aligned} \tag{5.14}$$

Writing this as

$$[1 + \Delta t\mathcal{L}]\eta_{t+\Delta t} = [1 + \Delta t\mathcal{R}]\eta_t, \tag{5.15}$$

where

$$\mathcal{L} = -\lambda_k[(a_1 - 1) - \lambda_k(1 - a_2)], \tag{5.16}$$

$$\mathcal{R} = -\lambda_k[(a_1 + \lambda_k a_2 - 3c^2) - a(c+1)(-1 - \lambda_k + 3c^2)]. \tag{5.17}$$

The von Neumann linear stability criterion leads to

$$\frac{|1 + \Delta t\mathcal{R}|}{|1 + \Delta t\mathcal{L}|} < 1, \tag{5.18}$$

which leads to

$$\frac{1 + \Delta t\mathcal{R}}{1 + \Delta t\mathcal{L}} < 1, \tag{5.19}$$

and

$$\frac{1 + \Delta t\mathcal{R}}{1 + \Delta t\mathcal{L}} > -1. \tag{5.20}$$

The inequality (5.19) implies $\mathcal{R} < \mathcal{L}$:

$$0 < \mathcal{L} - \mathcal{R} = -\lambda_k(ac + a + 1)(-1 - \lambda_k + 3c^2). \tag{5.21}$$

Because $ac + a + 1 > 0$, this recovers $-1 - \lambda_k + 3c^2 > 0$, which is the spinodal condition of the conserved dynamics [27]. To impose unconditional linear stability on the inequality (5.20), we want $\mathcal{R} + \mathcal{L} > 0$:

$$-\lambda_k[2a_1 - 1 - 3c^2 + a(c+1)(1 - 3c^2) - \lambda_k\{1 - 2a_2 - a(c+1)\}] > 0, \tag{5.22}$$

which implies that

$$\begin{aligned} a_1 &> \frac{1 + 3c^2 + a(c+1)(3c^2 - 1)}{2}, \\ a_2 &< \frac{1 + a(c+1)}{2}. \end{aligned} \tag{5.23}$$

Insisting on stability for all $c \in [-1, 1]$ and $a \in [0, 1]$, we obtain the global stability bounds for asymmetric bulk mobilities Eq.(5.13):

$$\begin{aligned} a_1 &> 4, \\ a_2 &< \frac{1}{2}. \end{aligned} \tag{5.24}$$

These bounds are more restrictive than the symmetric $a = 0$ case because of the range of asymmetries, but only for a_1. As with the symmetric algorithms, we expect the

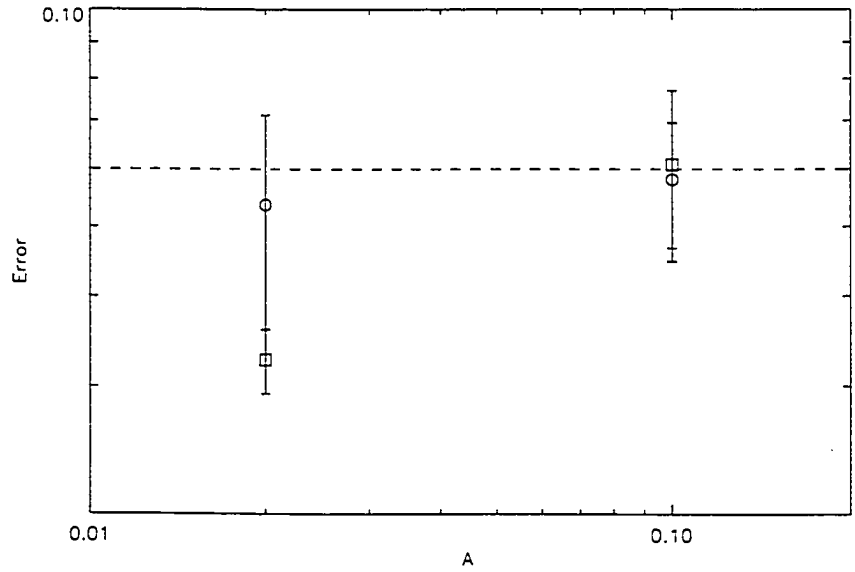

Figure 5.1: Plot of maximal difference of scaled structural factor vs A. The difference is obtained by comparison of scaled structural factor for conserved systems with Direct update ($\Delta t = At_s^{2/3}$) and asymmetric bulk mobilities ($R = 1/3$) with the same Direct update (same A) and symmetric bulk mobilities ($R = 1$), and averaged in the scaling regime. The system sizes are $L_{sys} = 256$ (at least 200 samples, open square, averaged over 4 times in $t_s \in [60, 200]$) and $L_{sys} = 512$ (at least 50 samples, open circle, averaged over 9 times in $t_s \in [60, 1600]$). The error bars are obtained as variances by averaging in the scaling regime.

greatest accuracy to be found for the smallest implicit terms. As a result, we choose values close to the threshold of inequality (5.24) for our numerical values: $a_1 = 5$ and $a_2 = 0$.

In order to detect the difference in correlations that are due to asymmetric bulk mobilities, we compare the correlations between algorithms with the same A to reduce the errors that result from the time-steps, and we control random errors in initial transients and finite-size effects by averaging large numbers of samples. Fig.5.1 shows a non-zero A-independent difference, as well as a small time-step errors that related to A. We will try smaller values of A and smaller values of R (more asymmetry) to get a larger resolved signal that are due to asymmetric bulk mobilities. We will also try asymmetric initial conditions (with $\langle\phi\rangle \neq 0$) to get an enhanced asymmetric signal.

5.1.2 Algorithms with asymmetric bulk diffusivities

Here we develop the algorithms for a study of universality classes of correlations with asymmetric bulk diffusivities, but leave a detailed numerical study for future work. In the bulk, $\nabla^2\phi \approx 0$ far from the interface, and using Eq.(5.1), we obtain

$$\mathbf{j} = -M(\phi_\pm)[\nabla V'(\phi_\pm)] = -D_\pm \nabla\phi, \tag{5.25}$$

where the bulk diffusivity is

$$D_\pm = M(\phi_\pm)V''(\phi_\pm). \tag{5.26}$$

Asymmetric bulk diffusivities $D_\pm$ can be characterized by the dimensionless ratio

$$R' \equiv \frac{D_-}{D_+} = \frac{M(\phi_-)V''(\phi_-)}{M(\phi_+)V''(\phi_+)}. \tag{5.27}$$

We will introduce asymmetric bulk diffusivities $D_\pm$ but symmetric bulk mobilities $M_\pm$ in the dynamics to test whether the scaled correlations only depend on asymmetric bulk mobilities as expected. We can introduce asymmetric bulk diffusivities only through asymmetric potentials, where the bulk mobilities $M(\phi_\pm) \equiv 1$. For our asymmetric potential $V_1(\phi)$, we want to retain the feature $V_1'(\phi) = 0$ for $\phi_\pm = \pm 1$ to maintain symmetric quenches when $\langle\phi\rangle = 0$, but we want $V_1''(\phi_+) \neq V_1''(\phi_-)$ for the

asymmetric bulk diffusivities. This is possible with (see Appendix G for other choices of potentials)

$$V_1(\phi) = \frac{1}{8}(\phi^2 - 1)^2(\phi^2 + 2b\phi + 1), \tag{5.28}$$

where $b \in [0, 1]$. This $V_1(\phi)$ has only two global minima at $\phi_\pm = \pm 1$. In fact

$$\begin{aligned} V_1'(\phi) &= \frac{1}{4}(\phi^2 - 1)(3\phi^3 + 5b\phi^2 + \phi - b) \\ &= \frac{1}{4}(3\phi^5 + 5b\phi^4 - 2\phi^3 - 6b\phi^2 - \phi + b) \end{aligned} \tag{5.29}$$

leads to only one real local maximum, so the potential retains the qualitative shape of a double-well potential. Also

$$V_1''(\phi) = \frac{1}{4}(15\phi^4 + 20b\phi^3 - 6\phi^2 - 12b\phi - 1), \tag{5.30}$$

so that $V_1''(\phi_\pm) = 2(1 \pm b)$, which by Eq.(5.27) leads to asymmetric mobilities

$$R' = \frac{1 - b}{1 + b}, \tag{5.31}$$

with $R' \in [0, 1]$ as $b \in [0, 1]$. Thus we get the same form as Eq.(5.12).

The dynamical equation with the asymmetric potential $V_1(\phi)$ is

$$\begin{aligned} \frac{\partial \phi}{\partial t} &= \nabla^2[-\nabla^2\phi + V'(\phi)], \\ &= \nabla^2\left[-\nabla^2\phi + \frac{1}{4}(3\phi^5 + 5b\phi^4 - 2\phi^3 - 6b\phi^2 - \phi)\right]. \end{aligned} \tag{5.32}$$

If we consider unconditionally stable algorithms with direct parameterizations, we need to introduce some implicit terms:

$$\begin{aligned} & \tilde{\phi}_{t+\Delta t} + \Delta t\nabla^2[(1 - a_1)\tilde{\phi}_{t+\Delta t} + (1 - a_2)\nabla^2\tilde{\phi}_{t+\Delta t}] \\ = \;& \phi_t + \Delta t\nabla^2(-a_1\phi_t - a_2\nabla^2\phi_t + \phi_t^3) \\ + \;& \Delta t\nabla^2\left[\phi_t - \phi_t^3 + \frac{1}{4}(3\phi_t^5 + 5b\phi_t^4 - 2\phi_t^3 - 6b\phi_t^2 - \phi_t)\right]. \end{aligned} \tag{5.33}$$

We want to do a von Neumann stability analysis for this equation, and obtain the conditions for a_1 and a_2. Linearizing this equation around $\phi(\mathbf{x}, t) \equiv c + \eta(\mathbf{x}, t)$, where $\phi = c$ is a constant phase, and taking its Fourier Transform, we obtain

$$\begin{aligned} & [1 - \Delta t\lambda_\mathbf{k}\{(a_1 - 1) - \lambda_\mathbf{k}(1 - a_2)\}]\eta_{\mathbf{k},t+\Delta t} \\ = \;& \left[1 - \Delta t\lambda_\mathbf{k}\left\{(a_1 + \lambda_\mathbf{k}a_2 - 1 - \frac{1}{4}(15c^4 + 20bc^3 - 6c^2 - 12bc - 1)\right\}\right]\eta_{\mathbf{k},t}. \end{aligned}$$

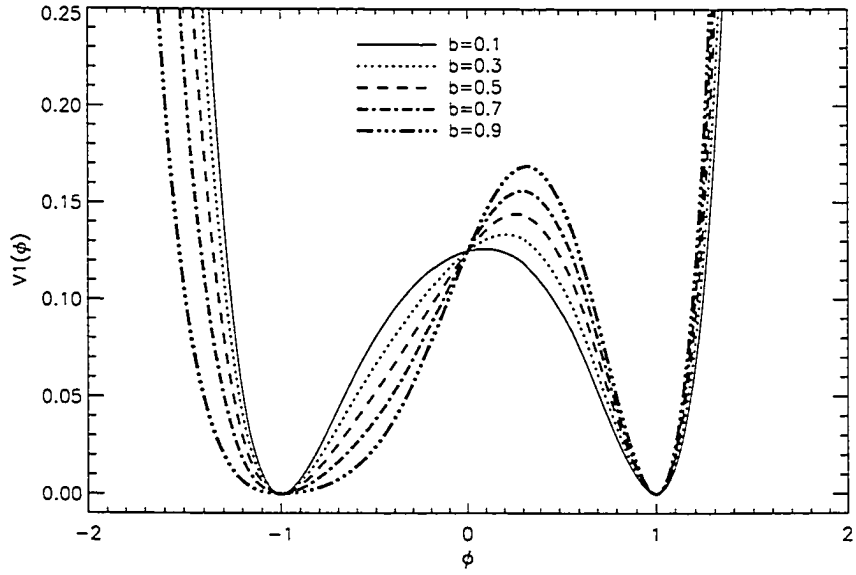

Figure 5.2: Plot of $V_1(\phi)$ vs ϕ, for different $b \in [0,1]$. We can see from the figure that larger values of b lead to local maximum at larger values of ϕ. V_1 always has two equal-depth local minima at $x = \pm 1$.

Writing this as

$$[1 + \Delta t\mathcal{L}]\eta_{t+\Delta t} = [1 + \Delta t\mathcal{R}]\eta_t, \tag{5.34}$$

where

$$\mathcal{L} = -\lambda_k[(a_1 - 1) - \lambda_k(1 - a_2)], \tag{5.35}$$

$$\mathcal{R} = -\lambda_k\left[(a_1 - 1) - \frac{1}{4}(15c^4 + 20bc^3 - 6c^2 - 12bc - 1) + \lambda_k a_2\right]. \tag{5.36}$$

The von Neumann linear stability criterion leads to

$$\frac{|1 + \Delta t\mathcal{R}|}{|1 + \Delta t\mathcal{L}|} < 1, \tag{5.37}$$

which leads to

$$\frac{1 + \Delta t\mathcal{R}}{1 + \Delta t\mathcal{L}} < 1, \tag{5.38}$$

and

$$\frac{1 + \Delta t\mathcal{R}}{1 + \Delta t\mathcal{L}} > -1. \tag{5.39}$$

The inequality (5.38) implies $\mathcal{R} < \mathcal{L}$:

$$0 < \mathcal{L} - \mathcal{R} = -\lambda_k\left[\frac{1}{4}(15c^4 + 20bc^3 - 6c^2 - 12bc - 1) - \lambda_k\right]. \tag{5.40}$$

which follows

$$\frac{1}{4}(15c^4 + 20bc^3 - 6c^2 - 12bc - 1) - \lambda_k > 0. \tag{5.41}$$

This is our spinodal condition, which is different from the standard spinodal condition $-1-\lambda_k+3c^2 > 0$ [27] since we used a different form of potential. Imposing $\mathcal{R}+\mathcal{L} > 0$ for unconditional linear stability, we have

$$-\lambda_k \left[2a_1 - 2 - \frac{1}{4}(15c^4 + 20bc^3 - 6c^2 - 12bc - 1) - \lambda_k(1 - 2a_2)\right] > 0, \tag{5.42}$$

which implies that

$$\begin{aligned} a_1 &> 1 + \frac{1}{8}(15c^4 + 20bc^3 - 6c^2 - 12bc - 1), \\ a_2 &< \frac{1}{2}. \end{aligned} \tag{5.43}$$

For $c \in [-1, 1]$ and $b \in [0, 1]$, the maximal value of $(15c^4 + 20bc^3 - 6c^2 - 12bc - 1)/8$ is 2. Thus the global bounds are:

$$\begin{aligned} a_1 &> 3, \\ a_2 &< \frac{1}{2}. \end{aligned} \tag{5.44}$$

We choose to do numerics with $a_1 = 4$ and $a_2 = 0$.

5.2 Anisotropic surface tension

Although the study of phase ordering dynamics has a long history, most of the work is confined to studies of isotropic surface tension. In general, the physical systems do not always have full rotational symmetry, and we need to consider anisotropic surface tension. Siegert [35] studied anisotropic surface tension in two-dimensional non-conserved systems and showed that anisotropy does not change the characteristic interfacial speeds. Recently, Rutenberg [36] showed that in two-dimensional conserved and non-conserved systems, with nonzero anisotropy, the correlation functions depend on the orientations in the scaling regime. Rutenberg and Vollmayr-Lee [37] solved a simplified coarsening system with arbitrary anisotropic surface tension and interface mobility, and found that the shapes of growing domains are anisotropic but different

from the equilibrium crystal shape. Anisotropic surface tension affects correlations in the scaling regime. While this indicates that anisotropy is relevant, nobody has yet investigated the universality classes that results from anisotropic surface tension. In principle our accelerated algorithms are ideal for this application. In this section, we develop the algorithms for a study of anisotropic surface tension, but leave a detailed numerical study for future work.

5.2.1 Algorithms with anisotropic surface tension

We want to implement surface tension anisotropy into systems as generally as possible in order to study a broad range of problems related to anisotropy. Recently several authors [38, 39, 40, 41] have introduced anisotropy into their systems. Here we introduce the method due to Kobayashi [42] and Wheeler, Murray and Schaefer [43], who include anisotropy by introducing a gradient energy coefficient $\epsilon(\theta)$ [44], which depend on the orientation θ of the gradient vector $\nabla\phi$, where

$$\theta = \tan^{-1}\left(\frac{\phi_y}{\phi_x}\right) \tag{5.45}$$

is the angle that $\nabla\phi \equiv (\phi_x, \phi_y)$ makes with the x axis. The angle θ is thus defined throughout the domain. The equations admit steady solutions of the form $\phi = \phi(\mathbf{g}\cdot\hat{\mathbf{n}})$, where $\hat{\mathbf{n}}$ is a constant unit vector and $\mathbf{g}$ is a coordinate normal to the domain wall. We have $\mathbf{g}\cdot\hat{\mathbf{n}} = x\cos\theta_0 + y\sin\theta_0$. The orientation is then constant, with $\theta = \theta_0$, and the solution is given by

$$\phi(g) = \tanh\left(\frac{\mathbf{g}\cdot\hat{\mathbf{n}}}{\sqrt{2}\epsilon(\theta_0)}\right). \tag{5.46}$$

The surface free energy for this orientation is then given by

$$\sigma(\theta_0) = \frac{2\sqrt{2}\epsilon(\theta_0)}{3}. \tag{5.47}$$

The above two results are obtained using Eq.(1.10) and Eq.(1.13).

We can also calculate the chemical potential for anisotropic interfacial energies as

$$\begin{aligned}\mu &\equiv \frac{\delta F}{\delta\phi} \\ &= -\nabla\cdot(\epsilon^2\nabla\phi) + \frac{\partial}{\partial x}\left(\epsilon\frac{d\epsilon}{d\theta}\frac{\partial\phi}{\partial y}\right) - \frac{\partial}{\partial y}\left(\epsilon\frac{d\epsilon}{d\theta}\frac{\partial\phi}{\partial x}\right) + \frac{dV}{d\phi},\end{aligned} \tag{5.48}$$

where the relation $\delta\theta = (\phi_x\delta\phi_y - \phi_y\delta\phi_x)/|\nabla\phi|^2$ is used. Using the relations

$$\begin{aligned} \theta_x &= (\phi_x\phi_{xy} - \phi_y\phi_{xx})/|\nabla\phi|^2, \\ \theta_y &= (\phi_x\phi_{yy} - \phi_y\phi_{xy})/|\nabla\phi|^2, \end{aligned} \tag{5.49}$$

if $\epsilon(\theta)$ is continuous everywhere, Eq.(5.48) can also be expressed in a form more suitable for computations [45],

$$\begin{aligned} \mu &= -\epsilon^2\nabla^2\phi - \epsilon\epsilon'[\sin(2\theta)(\phi_{yy} - \phi_{xx}) + 2\cos(2\theta)\phi_{xy}] \\ &\quad +\frac{1}{2}(\epsilon'^2 + \epsilon\epsilon'')[2\sin(2\theta)\phi_{xy} - \nabla^2\phi - \cos(2\theta)(\phi_{yy} - \phi_{xx})] + \frac{dV}{d\phi}, \end{aligned} \tag{5.50}$$

where $\epsilon' = d\epsilon/d\theta$, $\epsilon'' = d^2\epsilon/d\theta^2$, and the subscripts denote partial differentiation with respect to x or y.

Eq.(5.50) can be substituted into equations of motion Eq.(1.6) and Eq.(1.7) to describe conserved dynamics and non-conserved dynamics, respectively, for anisotropic surface tension.

5.2.2 von Neumann stability analysis

The von Neumann stability analysis for anisotropic surface tension is similar to the isotropic case. The difference is that we now have more terms and more parameters. Below we will show the von Neumann analysis for non-conserved dynamics.

Substituting Eq.(5.50) into the equation of motion for non-conserved dynamics, Eq.(1.7), and using $V(\phi) = (\phi^2 - 1)^2/4$, we get the non-conserved equation for anisotropic interfaces

$$\begin{aligned} \dot{\phi} &= \epsilon^2\nabla^2\phi + \epsilon\epsilon'[\sin(2\theta)(\phi_{yy} - \phi_{xx}) + 2\cos(2\theta)\phi_{xy}] \\ &\quad -\frac{1}{2}(\epsilon'^2 + \epsilon\epsilon'')[2\sin(2\theta)\phi_{xy} - \nabla^2\phi - \cos(2\theta)(\phi_{yy} - \phi_{xx})] + \phi - \phi^3. \end{aligned} \tag{5.51}$$

For a particular orientation θ, we can simplify the above equation as follows

$$\dot{\phi} = \phi + B_2(\theta)\phi_{xx} + B_3(\theta)\phi_{yy} + B_4(\theta)(\phi_{xx} + \phi_{yy} + 2\phi_{xy}) - \phi^3, \tag{5.52}$$

where

$$B_2(\theta) = \epsilon^2 + \frac{1}{2}(\epsilon'^2 + \epsilon\epsilon'') - \epsilon\epsilon'\sin(2\theta) - \frac{1}{2}(\epsilon'^2 + \epsilon\epsilon'')\cos(2\theta)$$

$$-\epsilon\epsilon' \cos(2\theta) + \frac{1}{2}(\epsilon'^2 + \epsilon\epsilon'') \sin(2\theta), \tag{5.53}$$

$$\begin{aligned} B_3(\theta) &= \epsilon^2 + \frac{1}{2}(\epsilon'^2 + \epsilon\epsilon'') + \epsilon\epsilon' \sin(2\theta) + \frac{1}{2}(\epsilon'^2 + \epsilon\epsilon'') \cos(2\theta) \\ &\quad -\epsilon\epsilon' \cos(2\theta) + \frac{1}{2}(\epsilon'^2 + \epsilon\epsilon'') \sin(2\theta), \end{aligned} \tag{5.54}$$

$$B_4(\theta) = \epsilon\epsilon' \cos(2\theta) - \frac{1}{2}(\epsilon'^2 + \epsilon\epsilon'') \sin(2\theta). \tag{5.55}$$

If we consider unconditionally stable algorithms, we need a general mix of implicit and explicit terms for the above equation:

$$\begin{aligned} &\phi_{t+\Delta t} + \Delta t\Big[(a_1 - 1)\phi_{t+\Delta t} + (a_2 - 1)B_2(\theta)\frac{\partial^2 \phi_{t+\Delta t}}{\partial x^2} + (a_3 - 1)B_3(\theta)\frac{\partial^2 \phi_{t+\Delta t}}{\partial y^2} \\ &+(a_4 - 1)B_4(\theta)\Big(\frac{\partial^2 \phi_{t+\Delta t}}{\partial x^2} + \frac{\partial^2 \phi_{t+\Delta t}}{\partial y^2} + 2\frac{\partial^2 \phi_{t+\Delta t}}{\partial x \partial y}\Big)\Big] \\ = \;& \phi_t + \Delta t\Big[a_1\phi_t + a_2 B_2(\theta)\frac{\partial^2 \phi_t}{\partial x^2} + a_3 B_3(\theta)\frac{\partial^2 \phi_t}{\partial y^2} \\ &+a_4 B_4(\theta)\Big(\frac{\partial^2 \phi_t}{\partial x^2} + \frac{\partial^2 \phi_t}{\partial y^2} + 2\frac{\partial^2 \phi_t}{\partial x \partial y}\Big) - \phi_t^3\Big]. \end{aligned} \tag{5.56}$$

Taking $\phi(\mathbf{x}, t) \equiv c + \eta(\mathbf{x}, t)$, linearizing Eq.(5.56) in η, and taking its Fourier Transform, we obtain

$$\begin{aligned} &[1 + \Delta t\{(a_1 - 1) - k_x^2 B_2(\theta)(a_2 - 1) - k_y^2 B_3(\theta)(a_3 - 1) \\ &-(k_x + k_y)^2 B_4(\theta)(a_4 - 1)\}]\eta_{\mathbf{k},t+\Delta t} \\ = \;& [1 + \Delta t\{a_1 - k_x^2 B_2(\theta)a_2 - k_y^2 B_3(\theta)a_3 - (k_x + k_y)^2 B_4(\theta)a_4 - 3c^2\}]\eta_{\mathbf{k},t} \end{aligned} \tag{5.57}$$

Writing this as

$$[1 + \Delta t\mathcal{L}]\eta_{t+\Delta t} = [1 + \Delta t\mathcal{R}]\eta_t. \tag{5.58}$$

Similar to von Neumann analysis for isotropic case, the necessary and sufficient condition for unconditional linear stability is

$$\mathcal{L} - \mathcal{R} > 0, \tag{5.59}$$

$$\mathcal{L} + \mathcal{R} > 0. \tag{5.60}$$

Firstly $\mathcal{L} - \mathcal{R} > 0$ yields:

$$0 < \mathcal{L} - \mathcal{R} = -1 + k_x^2 B_2(\theta) + k_y^2 B_3(\theta) + (k_x + k_y)^2 B_4(\theta) + 3c^2. \tag{5.61}$$

We can see that when $B_2(\theta) = B_3(\theta) = 1, B_4(\theta) = 0$, the above inequality recovers the spinodal condition of the non-conserved dynamics (3.4). Secondly $\mathcal{L} + \mathcal{R} > 0$ yields

$$\begin{aligned} 0 < \mathcal{L} + \mathcal{R} &= (2a_1 - 1 - 3c^2) - k_x^2 B_2(\theta)(2a_2 - 1) \\ &\quad -k_y^2 B_3(\theta)(2a_3 - 1) - (k_x + k_y)^2 B_4(\theta)(2a_4 - 1). \end{aligned} \tag{5.62}$$

If we impose the most restrictive value of $c \in [-1, 1]$, we get $2a_1 - 1 - 3c^2 > 0$. Also, we require the three terms $B_i(\theta)(2a_i - 1)$ in inequality (5.62) to be negative. This means the a_i are greater or smaller than $1/2$, depending on the signs of $B_i(\theta)$. In summary, the stability condition are:

$$\begin{aligned} a_1 &> 2, \\ a_i &< 1/2 \quad if \quad B_i(\theta) > 0, \\ a_i &> 1/2 \quad if \quad B_i(\theta) < 0. \end{aligned} \tag{5.63}$$

Since we do not know the sign for $B_i(\theta)$ in general, we should set $a_i = 1/2$, $(i = 2, 3, 4)$ to eliminate $B_i(\theta)$ from the stability condition. Therefore the stability condition for becomes

$$\begin{aligned} a_1 &> 2, \\ a_i &= \frac{1}{2}, \quad i = 2, 3, 4. \end{aligned} \tag{5.64}$$

The von Neumann analysis for conserved dynamics with anisotropic surface tension is quite similar to the non-conserved dynamics. We obtain the same stability condition (5.64) since the extra $-\lambda_{\mathbf{k}}$ term drops out of the stability equation.

Chapter 6

Summary and discussion

This chapter contains a summary of our results, and then discussion and some future research possibilities.

6.1 Summary

In Chapter 4, we obtain unconditionally stable accelerated algorithms ($\Delta t = At_s^{2/3}$) for conserved dynamics with arbitrary accuracy controlled by the size of the prefactor A. The relative multi-step error in scaled correlations with these accelerated algorithms scales as $\sqrt{A}$ (shown in Fig.4.4), which is consistent with our analysis in Chapter 4.

It is meaningful to explore the relative computational advantage offered by such an algorithm. In our simulations, we want to evolve the system as far as possible in the scaling regime, i.e. until largest possible $L(t_s)$. This means evolving until finite size effects, which is expected to appear when $L(t_s) \sim L_0 t_s^{1/3}$ is some fraction of the system size, so we define the simulation ending time t_{smax} by $L(t_{smax}) = fL_{sys}$, or

$$t_{smax} = \left(\frac{fL_{sys}}{L_0}\right)^3 = \left(\frac{f\Delta xN}{L_0}\right)^3 \tag{6.1}$$

where N is the linear size of the lattice, $\Delta x = 1$ is the lattice spacing, $f \approx 0.1$ reflects the fraction of the averaged domain size as finite size effects appear and $L_0 \approx 1.4$ [27]. With the fixed time-step ($\Delta t_{Eu} \approx 0.05$) Euler algorithm, evolving the system to t_{smax} requires the number of steps

$$n_{Eu} = \frac{t_{smax}}{\Delta t_{Eu}}. \tag{6.2}$$

On the other hand, with our accelerated algorithm $\Delta t = At_s^{2/3}$, evolving the system to t_{smax} needs the number of steps (see Eq.(4.53))

$$n_{Ac} = \frac{3t_{smax}^{1/3}}{A}. \tag{6.3}$$

Therefore the ratio of computer time cost is [27]

$$\frac{T_{Euler}}{T_{Direct}} = \frac{1}{\beta}\frac{n_{Eu}}{n_{Ac}}, \tag{6.4}$$

where β is the ratio of computer time per step

$$\beta = \frac{\tau_{Direct}}{\tau_{Euler}} \approx 2.5. \tag{6.5}$$

Combining all these relations, we obtain the relative speedup of this algorithm with respect to the Euler algorithm as [27]

$$\frac{T_{Euler}}{T_{Direct}} = \frac{A}{3\beta\Delta t_{Eu}}\left(\frac{f\Delta x N}{L_0}\right)^2 \sim N^2, \tag{6.6}$$

which is of order N^2, indicating that we will gain dramatic speedup as N is larger.

Unlike the Euler algorithm, in these accelerated algorithms in conserved systems ($\Delta t = At_s^{2/3}$), we have a Δt- and k-dependent effective time-step Δt_{eff} Eq.(4.9) — the effective time-step is not the same for each mode. The structural time-step Δt_s Eq.(4.19) and Eq.(4.22) can be considered as the integrated "effect" of the effective time-step over all modes. It is interesting to note that the difference between Δt_{eff} and Δt_s corresponds to the single-step error in Fourier-space (see Eq.(4.56) and Eq.(4.85)). We have not obtained a significant speedup for non-conserved systems — the maximum relative speedup factor is roughly 1.45 with parameters $a_1 \to 2^+$ and $a_2 \to 0.5^-$.

The structural time t_s and structural time-step Δt_s play crucial role in determining the "real acceleration" since structural time is the only probe of how fast the algorithm actually evolves the system structure. Conversely, the algorithmic time-step Δt is not meaningful except in the expression of the effective step Δt_{eff} and in the discussion of accuracy. It is by rigorously distinguishing Δt and Δt_s that we were able to understand these algorithms more clearly.

6.2 Discussion

Why is the Euler algorithm wastefully accurate at late times? By studying the asymptotic scaling of field derivatives in both real space and Fourier space, we can see that

the multi-step error is decreasing with time, thus making it more and more accurate, i.e., wastefully accurate. As an illustration, consider the single-step error of Euler update (fixed Δt_{Eu}) with respect to the actual conserved dynamics in real space

$$\Delta\tilde{\phi} = \Delta t_{Eu}\dot{\phi} - \sum_{n=1}^{\infty} \frac{\partial_t^n \phi}{n!} \Delta t_s^n, \tag{6.7}$$

$$= -\sum_{n=2}^{\infty} \frac{\partial_t^n \phi}{n!} \Delta t_{Eu}^n, \tag{6.8}$$

$$\sim \frac{\partial^2 \phi}{\partial t^2}, \tag{6.9}$$

$$\sim t_s^{-5/3}, \tag{6.10}$$

where the field scaling in real space $\partial_t^n \phi \sim t_s^{-1/3-2n/3}$ [27] and $\Delta t_s = \Delta t_{Eu}$ are used. Evolving the system until t_s requires $t_s/\Delta t_{Eu}$ updates, which, following the argument of multi-step error in Chapter 4, indicates that the multi-step error is at most $O(t_s^{-2/3})$. Thus the Euler algorithm is more and more accurate as time evolves. More generally, since an accelerated scheme of $\Delta t = A t_s^{\beta}$ will have a constant multi-step error only if $\beta = 2/3$, any scheme with $\beta < 2/3$ will lead to a multi-step error that decreases towards 0 at late times, and so will be wastefully accurate.

Another question related to these accelerated algorithm is which parameters a_1 and a_2 make the algorithm most efficient. The answer to this question in non-conserved systems is quite clear from Eq.(4.82). As $a_1 \to 2^+$ and $a_2 \to 0.5^-$ at the stability boundary, this algorithm gives a maximum Δt_s and the smallest errors. In conserved systems, Eq.(4.27) and Eq.(4.28) indicates that a_2 does not contribute so is not of interest, at least in the scaling regime. For fixed prefactor A, the smaller the value of a_1, the larger the Δt_s, the smaller the error. Therefore as $a_1 \to 2^+$, this scheme approaches maximum speedup.

It is interesting to compare the time it takes to reach finite-size effect in both systems. With $\Delta t \sim t_s^{\alpha}$, the number of steps to get to the finite-size effect in conserved dynamics is

$$n_{CO} \sim N^{3(1-\alpha)}, \tag{6.11}$$

while for non-conserved dynamics it is

$$n_{NC} \sim N^{2(1-\alpha)}, \tag{6.12}$$

where $N = L_{sys}/\Delta x$ is the linear lattice size. $n_{NC} \sim N^2$ as $\Delta t_s = const$ in non-conserved dynamics, and $n_{CO} \sim N$ as $\Delta t_s \sim t_s^{2/3}$ in conserved dynamics. This indicates that we spend much less time reaching finite-size effect in conserved dynamics than in non-conserved dynamics using our accelerated algorithms.

We expect these accelerated algorithms to have extensive application in various systems. The implementation of these accelerated algorithms is straightforward. First we semi-implicitly parameterize the dynamics, then we do a von Neumann linear stability analysis and determine the constraints for the parameters. We then need to check numerically the unconditional stability of specific von Neumann stable systems, as per Section 3.3. The last thing we need to check is the accuracy — we need to know whether the multi-step error can be controlled at arbitrary accuracy. It is helpful but not essential to know the physics behind the system under study since it helps us to pick the appropriate algorithmic time-step Δt. The combination of Δt_s and errors related to correlations are useful in choosing the right time-step Δt. The obvious systems for future study are hydrodynamic models [16].

Appendix A

"Checkerboard instability" for Euler algorithm

For the Euler algorithm in the study of partial differential equations, there is a threshold for the time-step Δt, above which the simulation becomes unstable. This is the checkerboard instability [19] which forces one to use a fixed value time-step. In this Appendix we study this threshold in both non-conserved and conserved two-dimensional systems by doing a von Neumann linear stability analysis. We will also see the spinodal condition is a natural outcome of this analysis.

In two-dimensional, a discrete form of Laplacian $\nabla^2\eta(x,y)$ can be written as

$$\begin{aligned}\nabla^2\eta(x,y) &= \alpha\Big[\frac{\eta(x+\Delta x,y)+\eta(x-\Delta x,y)-2\eta(x,y)}{\Delta^2 x} \\ &\quad +\frac{\eta(x,y+\Delta y)+\eta(x,y-\Delta y)-2\eta(x,y)}{\Delta^2 y}\Big] \\ &+ \beta\Big[\frac{\eta(x+\Delta x,y+\Delta y)+\eta(x-\Delta x,y-\Delta y)-2\eta(x,y)}{\Delta^2 x+\Delta^2 y} \\ &\quad +\frac{\eta(x-\Delta x,y+\Delta y)+\eta(x+\Delta x,y-\Delta y)-2\eta(x,y)}{\Delta^2 x+\Delta^2 y}\Big], \qquad \text{(A.1)}\end{aligned}$$

where Δx and Δy are lattice spacing in x and y direction, α $(0 \le \alpha \le 1)$ is associated with the nearest neighbor terms and β $(0 \le \beta \le 1)$ is associated with the second nearest neighbor terms, and with the relation $\alpha + \beta = 1$. In our study, we let $\Delta x = \Delta y = 1$. Now x and y are integers ranging from 0 to $L-1$, where L is the system size. We have

$$\begin{aligned}\nabla^2\eta(x,y) &= \alpha[\eta(x+1,y)+\eta(x-1,y)+\eta(x,y+1)+\eta(x,y-1)-4\eta(x,y)] \\ &\quad +\frac{\beta}{2}[\eta(x+1,y+1)+\eta(x-1,y+1)+\eta(x+1,y-1) \\ &\quad +\eta(x-1,y-1)-4\eta(x,y)]. \qquad \text{(A.2)}\end{aligned}$$

In the discrete form, we can write

$$\eta(x,y) \equiv \sum_{k_x}\sum_{k_y} e^{2\pi i(k_x x+k_y y)/L}\eta(k_x,k_y). \qquad \text{(A.3)}$$

For non-conserved dynamics, taking $\phi(\mathbf{x},t) \equiv c + \eta(\mathbf{x},t)$, we linearize Eq.(1.7) to get

$$\dot{\eta} = \nabla^2\eta + \eta - 3c^2\eta. \tag{A.4}$$

Substituting Eq.(A.3) and Eq.(A.2) into Eq.(A.4), we have

$$\begin{aligned}
& \dot{\eta}(k_x,k_y,t) \\
= \;& \alpha[e^{2\pi ik_x/L} + e^{-2\pi ik_x/L} + e^{2\pi ik_y/L} + e^{-2\pi ik_y/L} - 4]\eta(k_x,k_y,t) \\
& + \frac{\beta}{2}[e^{2\pi i(k_x+k_y)/L} + e^{-2\pi i(k_x+k_y)/L} + e^{2\pi i(k_x-k_y)/L} + e^{-2\pi i(k_x-k_y)/L} - 4]\eta(k_x,k_y,t) \\
& + (1-3c^2)\eta(k_x,k_y,t), \\
= \;& 2\alpha[\cos(2\pi k_x/L) + \cos(2\pi k_y/L) - 2]\eta(k_x,k_y,t) \\
& + \beta[\cos(2\pi(k_x+k_y)/L) + \cos(2\pi(k_x-k_y)/L) - 2]\eta(k_x,k_y,t) \\
& + (1-3c^2)\eta(k_x,k_y,t), \\
= \;& (\lambda_{\mathbf{k}} + 1 - 3c^2)\eta(k_x,k_y,t),
\end{aligned} \tag{A.5}$$

where

$$\begin{aligned}
\lambda_{\mathbf{k}} &= -2\alpha\left[2 - \cos\frac{2\pi k_x}{L} - \cos\frac{2\pi k_y}{L}\right] - \beta\left[2 - \cos\frac{2\pi(k_x+k_y)}{L} - \cos\frac{2\pi(k_x-k_y)}{L}\right], \\
&= -4\alpha\left[\sin^2\frac{\pi k_x}{L} + \sin^2\frac{\pi k_y}{L}\right] - 2\beta\left[\sin^2\frac{\pi(k_x+k_y)}{L} + \sin^2\frac{\pi(k_x-k_y)}{L}\right], \\
&\geq -8\alpha - 4\beta, \\
&= -4\alpha - 4,
\end{aligned} \tag{A.6}$$

On the other hand, we have

$$\dot{\eta}(k_x,k_y,t) = \frac{\eta(k_x,k_y,t+\Delta t) - \eta(k_x,k_y,t)}{\Delta t}. \tag{A.7}$$

Substituting Eq.(A.7) into Eq.(A.5), we get

$$\frac{\eta(k_x,k_y,t+\Delta t)}{\eta(k_x,k_y,t)} = (\lambda_{\mathbf{k}} + 1 - 3c^2)\Delta t + 1. \tag{A.8}$$

The linear stability criterion requires that

$$|\eta(k_x,k_y,t+\Delta t)| < |\eta(k_x,k_y,t)|, \tag{A.9}$$

which implies that

$$(\lambda_{\mathbf{k}} + 1 - 3c^2)\Delta t + 1 < 1, \tag{A.10}$$

and

$$(\lambda_k + 1 - 3c^2)\Delta t + 1 > -1. \tag{A.11}$$

The inequality (A.10) recovers the spinodal condition inequality (3.4). The inequality (A.11) shows the checkerboard instability for the Euler update; i.e. Δt most be below a threshold to maintain stability:

$$\Delta t < \frac{2}{3c^2 - 1 - \lambda_k}. \tag{A.12}$$

The threshold for Δt is k-dependent, and we want to find a threshold that satisfies every mode. Using inequality (A.6) and $c^2 \leq 1$, we obtain

$$\Delta t = \frac{2}{4\alpha + 4 + 2} = \frac{1}{2\alpha + 3}. \tag{A.13}$$

Note that when α is taken extreme values 1 and 0, the right hand side is 1/5 and 1/3, respectively. In the code we are currently using, we use $\alpha = 2/3$ for isotropy, and we have $\Delta t \leq 0.23$ for stability. Numerically we always use $\Delta t = 0.2$ in non-conserved systems throughout this thesis.

For conserved dynamics, linearizing Eq.(1.6), we get

$$\dot{\eta} = -\nabla^2(\nabla^2\eta + \eta - 3c^2\eta). \tag{A.14}$$

Likewise, we can get an equation analogous to Eq.(A.5)

$$\dot{\eta}(k_x, k_y, t) = -\lambda_k(\lambda_k + 1 - 3c^2)\eta(k_x, k_y, t). \tag{A.15}$$

Similar to non-conserved case, we get

$$\Delta t < \frac{2}{-\lambda_k(3c^2 - 1 - \lambda_k)}, \tag{A.16}$$

and we choose

$$\Delta t = \frac{2}{(4\alpha + 4)(4\alpha + 4 + 2)} = \frac{1}{(4\alpha + 4)(2\alpha + 3)}, \tag{A.17}$$

which satisfies every mode. Note that when α is taken extreme values 1 and 0, the right hand side is 1/40 and 1/12, respectively, which are smaller than in non-conserved case. In the code we are currently using, where $\alpha = 2/3$, we have $\Delta t \leq 0.034$ for stability. Numerically we always use $\Delta t = 0.03$ in conserved systems throughout this thesis.

Appendix B

Finite-size effects

During the evolution of a finite system, there are three different regimes (see Fig.1.2): the first is a transient period, during which the domain size is nearly stationary and the order parameters saturate into one of the two equilibrium states, followed by a scaling regime during which the domain size $L(t)$ increases with a power law in time, $L(t) \sim t^{\alpha}$. When the domain size $L(t)$ reaches a fraction of the system size L_{sys}, finite-size effects appear, which will cause the domain size to deviate from the power law. In our simulation, we usually ignore the transient period ($0 < t < 10$), i.e., we take our data starting from $t \approx 10$ until the finite-size effect becomes significant. Fig.B.1 illustrate the effect. Among these regimes, we are only interested in the scaling regime. Therefore, we halt the simulation when the system is in the finite-size effect for computational efficiency. Estimated maximal times for various system sizes are outlined in Table B.1 for non-conserved and in Table B.2 for conserved dynamics.

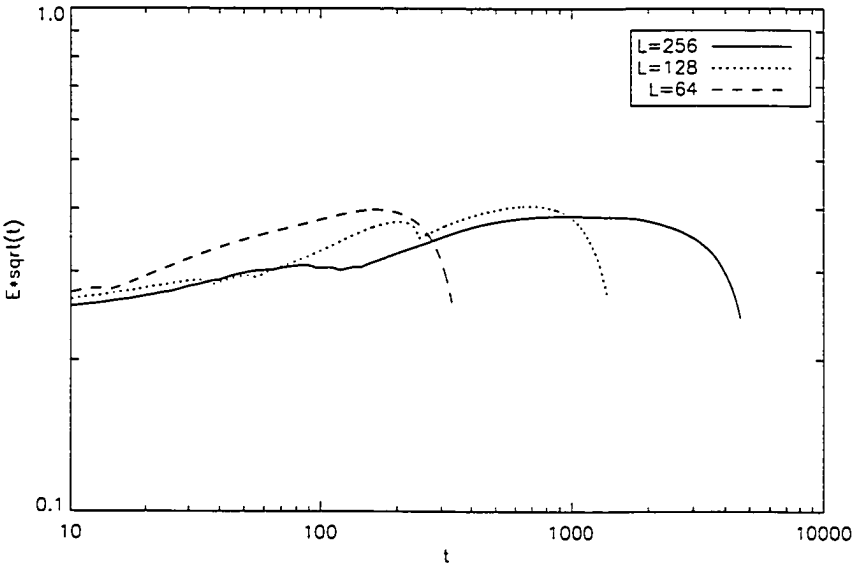

Figure B.1: Plot of $Et^{1/2}$ as a function of time t, where E is the energy density, with an Euler update with a fixed time step $\Delta t = 0.2$ in non-conserved systems, with three different system sizes $L_{sys} = 64, 128$ and 256. We can see the finite-size effect for different system sizes: the bigger the system size, the longer the finite-size effect. Since in non-conserved systems, $E \sim 1/L \sim t^{-1/2}$ in scaling regime, we have $Et^{1/2} \sim const.$ Finite-size effect appears as $Et^{1/2}$ deviates from a constant.

L_{sys}	t_{max}
64	8
128	32
256	128
512	512
1024	2048
2048	8192

Table B.1: Estimated maximal time t_{max} that a system can evolve before finite-size appears for both energy density E and scaled correlation function, for different linear system sizes L_{sys} in non-conserved systems. Since $L(t) \sim t^{1/2}$ for non-conserved systems, we have $t_{max} \sim L_{sys}^2$. Therefore, we will expect evolving the system 4 times longer to reach finite-size effect if we double the linear system size. We use this table as a guideline in non-conserved systems throughout this thesis.

L_{sys}	t_{max}
64	4
128	32
256	256
512	2048
1024	16384
2048	131072

Table B.2: Estimated maximal time t_{max} that a system can evolve before finite-size appears for both energy density E and scaled correlation function, for different linear system sizes L_{sys} in conserved systems. Since $L(t) \sim t^{1/3}$ for conserved systems, we have $t_{max} \sim L_{sys}^3$. Therefore, we will expect evolving the system 8 times longer to reach finite-size effect if we double the linear system size. We use this table as a guideline in conserved systems throughout this thesis.

Appendix C

FFT algorithm for calculating correlations

While standard, the algorithm of Fast Fourier Transform (FFT) for calculating the correlation function and its Fourier transform, the structure factor, is by no means transparent. It is therefore useful to explicitly explain how it works to help any debugging.

We have a two-dimensional discrete array of the order parameter $\phi_x(n_1, n_2)$, where n_1 and n_2 are integers ranging from 0 to $L-1$, and L is the system size 2^m (with m being a positive integer for FFT). In order to calculate the correlations, it is necessary to obtain $\phi_k(n_1, n_2)$, which is the explicit form of the discrete Fourier Transform of array $\phi_x(n_1, n_2)$. In "Numerical Recipes in C" [28], there is a standard routine rlft3 for this. I will introduce this routine and show how the correlations can be obtained.

The input data $\phi_x(n_1, n_2)$ is stored as a real, three-dimensional array data[1..1][1..L][1..L], with the first dimension vanishes

$$\mathsf{data}[1][\mathsf{i}_1][\mathsf{i}_2] = \phi_x(i_1 - 1, i_2 - 1) \quad i_1, i_2 \in [1, L]. \tag{C.1}$$

After FFT, the output data $\phi_k(n_1, n_2)$ comes as a complex, three dimensional array SPEC[1..1][1..L][1..$L/2+1$]. The subscript range SPEC[1..1][1..L][1..$L/2$] is returned in the input array data[1..1][1..L][1..L] with the correspondence

$$\begin{aligned} Re(\mathsf{SPEC}[1][\mathsf{i}_1][\mathsf{i}_2]) &= \mathsf{data}[1][\mathsf{i}_1][2 * \mathsf{i}_2 - 1], \\ Im(\mathsf{SPEC}[1][\mathsf{i}_1][\mathsf{i}_2]) &= \mathsf{data}[1][\mathsf{i}_1][2 * \mathsf{i}_2], \end{aligned} \tag{C.2}$$

with $i_1 \in [1, L]$ and $i_2 \in [1, L/2]$. The remaining SPEC[1..1][1..L][$L/2+1$] is returned in the two-dimensional array speq[1..1][1..$2 * L$], with the correspondence

$$\begin{aligned} Re(\mathsf{SPEC}[1][\mathsf{i}_1][\mathsf{L}/2 + 1]) &= \mathsf{speq}[1][2 * \mathsf{i}_1 - 1], \\ Im(\mathsf{SPEC}[1][\mathsf{i}_1][\mathsf{L}/2 + 1]) &= \mathsf{speq}[1][2 * \mathsf{i}_1], \end{aligned} \tag{C.3}$$

with $i_1 \in [1, L]$. To summary, we obtain $\phi_k(n_1, n_2)$ as

$$\phi_k(i_1 - 1, i_2 - 1) =$$

$$\begin{cases} \mathsf{data[1][i_1][2*i_2-1]} + i * \mathsf{data[1][i_1][2*i_2]} & i_1 \in [1, L], i_2 \in [1, L/2] \\ \mathsf{speq[1][2*i_1-1]} + i * \mathsf{speq[1][2*i_1]} & i_1 \in [1, L], i_2 = L/2+1 \\ \mathsf{data[1][1][2*(L+2-i_2)-1]} & \\ \quad -i * \mathsf{data[1][1][2*(L+2-i_2)]} & i_1 = 1, i_2 \in [L/2+2, L] \\ \mathsf{data[1][L+2-i_1][2*(L+2-i_2)-1]} & \\ \quad -i * \mathsf{data[1][L+2-i_1][2*(L+2-i_2)]} & i_1 \in [2, L], i_2 \in [L/2+2, L] \end{cases}$$

where $\phi_k(i_1 - 1, i_2 - 1)$ with $i_1 \in [1, L]$ and $i_2 \in [L/2 + 2, L]$ terms are obtained in such a way that $\phi_k(n_1, n_2)$ is complex conjugate symmetric at $\phi_k(L/2, L/2)$. Now we can obtain the structure factor

$$\begin{aligned} S_k(n_1, n_2) &\equiv \phi_k(n_1, n_2)\phi_k(-n_1, -n_2), \\ &= \phi_k(n_1, n_2)\phi_k(L - n_1, L - n_2), \\ &= Re^2\phi_k(n_1, n_2) + Im^2\phi_k(n_1, n_2), \end{aligned} \tag{C.4}$$

as

$$S_k(i_1 - 1, i_2 - 1) =$$

$$\begin{cases} \mathsf{data^2[1][i_1][2*i_2-1]} + \mathsf{data^2[1][i_1][2*i_2]} & i_1 \in [1, L], i_2 \in [1, L/2] \\ \mathsf{speq^2[1][2*i_1-1]} + \mathsf{speq^2[1][2*i_1]} & i_1 \in [1, L], i_2 = L/2+1 \\ \mathsf{data^2[1][1][2*(L+2-i_2)-1]} & \\ \quad +\mathsf{data^2[1][1][2*(L+2-i_2)]} & i_1 = 1, i_2 \in [L/2+2, L] \\ \mathsf{data^2[1][L+2-i_1][2*(L+2-i_2)-1]} & \\ \quad +\mathsf{data^2[1][L+2-i_1][2*(L+2-i_2)]} & i_1 \in [2, L], i_2 \in [L/2+2, L] \end{cases}$$

The array $S_k(n_1, n_2)$ is symmetric at $S_k(L/2, L/2)$, and we have $S_k(n_1, n_2) = S_k(L - n_1, L - n_2)$.

If we want to obtain correlation function $C_x(n_1, n_2)$, which is the Fourier transform of structure factor $S_k(n_1, n_2)$, we need fill in the arrays rdata[1..1][1..L][1..L] and rspeq[1..1][1..$2 * L$] for inverse FFT. Because S_k is real, the imaginary parts of the correlation function C_x is zero. Therefore, we can fill in as follows

$$\begin{aligned} \mathsf{rdata}[1..1][1..\mathsf{i}_1][2*\mathsf{i}_2-1] &= \mathsf{data}^2[1][\mathsf{i}_1][2*\mathsf{i}_2-1] + \mathsf{data}^2[1][\mathsf{i}_1][2*\mathsf{i}_2], \\ \mathsf{rdata}[1..1][1..\mathsf{i}_1][2*\mathsf{i}_2] &= 0, \end{aligned}$$

with $i_1 \in [1, L]$ and $i_2 \in [1, L/2]$, and

$$\begin{aligned} \mathsf{rspeq}[1..1][2*\mathsf{i}_1-1] &= \mathsf{speq}^2[1][2*\mathsf{i}_1-1] + \mathsf{speq}^2[1][2*\mathsf{i}_1], \\ \mathsf{rspeq}[1..1][2*\mathsf{i}_1] &= 0, \end{aligned}$$

with $i_1 \in [1, L]$. Thus combine rdata[1..1][1..L][1..L] and rspeq[1..1][1..$2 * L$], we will be able to form a complex, three dimensional array RSPEC[1..1][1..L][1..$L/2 + 1$] for inverse FFT

$$\begin{aligned} Re(\mathsf{RSPEC}[1][\mathsf{i}_1][\mathsf{i}_2]) &= \mathsf{rdata}[1][\mathsf{i}_1][2*\mathsf{i}_2-1], \\ Im(\mathsf{RSPEC}[1][\mathsf{i}_1][\mathsf{i}_2]) &= \mathsf{rdata}[1][\mathsf{i}_1][2*\mathsf{i}_2], \end{aligned} \tag{C.5}$$

with $i_1 \in [1, L]$ and $i_2 \in [1, L/2]$, and

$$\begin{aligned} Re(\mathsf{RSPEC}[1][\mathsf{i}_1][\mathsf{L}/2+1]) &= \mathsf{rspeq}[1][2*\mathsf{i}_1-1], \\ Im(\mathsf{RSPEC}[1][\mathsf{i}_1][\mathsf{L}/2+1]) &= \mathsf{rspeq}[1][2*\mathsf{i}_1], \end{aligned} \tag{C.6}$$

with $i_1 \in [1, L]$. After inverse FFT, rlft3 routine will transform the complex, three dimensional array RSPEC[1..1][1..L][1..$L/2+1$] to the array rdata[1..1][1..L][1..L], which corresponds with $C_x(n_1, n_2)$ as

$$C_x(i_1 - 1, i_2 - 1) = \mathsf{rdata}[1][\mathsf{i}_1][\mathsf{i}_2] \quad i_1, i_2 \in [1, L]. \tag{C.7}$$

The array $C_x(n_1, n_2)$ is symmetric at $C_x(L/2, L/2)$, and we have $C_x(n_1, n_2) = C_x(L - n_1, L - n_2)$.

Appendix D

Test of correlation function and structure factor

It is important to test the structure and make sure the FFT works. We find a good test of numerical algorithm is "white-noise", which is a typical example of a completely disordered configuration of order parameter. In a two-dimensional system, we have

$$\langle \phi(\mathbf{x})\phi(\mathbf{x}')\rangle = \Delta\delta(\mathbf{x}-\mathbf{x}'), \tag{D.1}$$

with $\mathbf{x} = n_1\mathbf{i}+n_2\mathbf{j}$, where n_1 and n_2 are integers ranging from 0 to $L-1$. $\langle ...\rangle$ represents an average over different systems, and Δ controls the size of the fluctuation in ϕ. We characterize the "noise" by its moments

$$\begin{aligned} \langle \phi(\mathbf{x})\rangle &= 0, \\ \langle \phi^2(\mathbf{x})\rangle &= A, \\ \langle \phi^4(\mathbf{x})\rangle &= B, \end{aligned} \tag{D.2}$$

where A and B are constants depending on the details of the distribution, and

$$C(\mathbf{r}) \equiv \langle \phi(\mathbf{x}+\mathbf{r})\phi(\mathbf{x})\rangle = \begin{cases} 0 & \text{if } \mathbf{r}\neq 0 \\ A & \text{if } \mathbf{r}=0 \end{cases} \tag{D.3}$$

Thus, we can calculate the Fourier transform of $\phi(\mathbf{x})$ and structure factor as

$$\phi_{\mathbf{k}} \equiv \frac{1}{L}\sum_{\mathbf{x}} e^{-2\pi i\mathbf{k}\cdot\mathbf{x}/L}\phi(\mathbf{x}), \tag{D.4}$$

$$S(\mathbf{k}) \equiv \phi_{\mathbf{k}}\phi_{-\mathbf{k}}. \tag{D.5}$$

We can now calculate the average value of structure factor $S(\mathbf{k})$ as

$$\begin{aligned} \langle S(\mathbf{k})\rangle &= \langle \phi_{\mathbf{k}}\phi_{-\mathbf{k}}\rangle, \\ &= \frac{1}{L^2}\sum_{\mathbf{x}}\sum_{\mathbf{x}'} e^{-2\pi i\mathbf{k}\cdot(\mathbf{x}-\mathbf{x}')/L}\langle \phi(\mathbf{x})\phi(\mathbf{x}')\rangle, \\ &= A. \end{aligned} \tag{D.6}$$

Next we calculate the average value of $S^2(\mathbf{k})$ as

$$\begin{aligned}
\langle S^2(\mathbf{k})\rangle &= \langle \phi_{\mathbf{k}}\phi_{-\mathbf{k}}\phi_{\mathbf{k}}\phi_{-\mathbf{k}}\rangle, \\
&= \frac{1}{L^4}\sum_{\mathbf{x}}\sum_{\mathbf{x}'}\sum_{\mathbf{x}''}\sum_{\mathbf{x}'''} e^{-2\pi i\mathbf{k}\cdot(\mathbf{x}-\mathbf{x}'+\mathbf{x}''-\mathbf{x}''')/L}\langle\phi(\mathbf{x})\phi(\mathbf{x}')\phi(\mathbf{x}'')\phi(\mathbf{x}'''),\rangle \\
&= \frac{1}{L^4}\sum_{\mathbf{x}=\mathbf{x}',\mathbf{x}''=\mathbf{x}''',\mathbf{x}\neq\mathbf{x}''}\langle\phi^2(\mathbf{x})\rangle\langle\phi^2(\mathbf{x}'')\rangle + \frac{1}{L^4}\sum_{\mathbf{x}=\mathbf{x}''',\mathbf{x}'=\mathbf{x}'',\mathbf{x}\neq\mathbf{x}'}\langle\phi^2(\mathbf{x})\rangle\langle\phi^2(\mathbf{x}')\rangle \\
&\quad + \frac{1}{L^4}\sum_{\mathbf{x}=\mathbf{x}'',\mathbf{x}'=\mathbf{x}''',\mathbf{x}\neq\mathbf{x}'} e^{-4\pi i\mathbf{k}\cdot(\mathbf{x}-\mathbf{x}')/L}\langle\phi^2(\mathbf{x})\rangle\langle\phi^2(\mathbf{x}')\rangle \\
&\quad + \frac{1}{L^4}\sum_{\mathbf{x}=\mathbf{x}'=\mathbf{x}''=\mathbf{x}'''}\langle\phi^4(\mathbf{x})\rangle, \\
&= 2A^2 - \frac{2A^2}{L^2} + \frac{B}{L^2} + \frac{A^2}{L^4}\sum_{\mathbf{x}\neq\mathbf{x}'} e^{-4\pi i\mathbf{k}\cdot(\mathbf{x}-\mathbf{x}')/L}. \qquad \text{(D.7)}
\end{aligned}$$

Note that in the two extreme cases of $\mathbf{k}$; i.e. $\mathbf{k}=0$ and $\mathbf{k}=\frac{L}{2}\mathbf{i}+\frac{L}{2}\mathbf{j}$, we have $e^{-4\pi i\mathbf{k}\cdot(\mathbf{x}-\mathbf{x}')/L}=1$ and

$$\langle S^2(0,0)\rangle = \langle S^2(L/2,L/2)\rangle = 3A^2 - \frac{3A^2}{L^2} + \frac{B}{L^2}. \qquad \text{(D.8)}$$

We continue our calculation of $\langle S^2(\mathbf{k})\rangle$ for other $\mathbf{k}$ as

$$\begin{aligned}
\langle S^2(\mathbf{k})\rangle &= 2A^2 - \frac{2A^2}{L^2} + \frac{B}{L^2} + \frac{A^2}{L^4}\left(\sum_{n_1\neq n_1'}\sum_{n_2,n_2'} + \sum_{n_1=n_1'}\sum_{n_2\neq,n_2'}\right) e^{-4\pi i[k_1(n_1-n_1')+k_2(n_2-n_2')]/L} \\
&= 2A^2 - \frac{2A^2}{L^2} + \frac{B}{L^2} \\
&+ \frac{A^2}{L^4}\sum_{n_1''=1}^{L-1}(L-n_1'')(e^{-4\pi ik_1n_1''/L} + e^{4\pi ik_1n_1''/L}) \\
&\quad \times\left[\sum_{n_2''=1}^{L-1}(L-n_2'')(e^{-4\pi ik_2n_2''/L} + e^{4\pi ik_2n_2''/L}) + L\right] \\
&+ \frac{A^2}{L^4}L\sum_{n_2''=1}^{L-1}(L-n_2'')(e^{-4\pi ik_2n_2''/L} + e^{4\pi ik_2n_2''/L}) \qquad \text{(D.9)}
\end{aligned}$$

where $n_1''=n_1-n_1'$ and $n_2''=n_2-n_2'$. Note that $\cos(4\pi k_1n_1''/L)=\cos(4\pi k_1(L-n_1'')/L)$, we have

$$\sum_{n_1''=1}^{L-1}(L-n_1'')(e^{-4\pi ik_1n_1''/L} + e^{-4\pi ik_1n_1''/L})$$

$$
\begin{aligned}
&= 2\sum_{n_1''=1}^{L-1}(L-n_1'')\cos(4\pi k_1 n_1''/L), \\
&= 2L\sum_{n_1''=1}^{L/2-1}\cos(4\pi k_1 n_1''/L)+L, \\
&= 2L\cos((L/2)2\pi k_1/L)\sin((L/2-1)2\pi k_1/L)/\sin(2\pi k_1/L)+L, \\
&= 2L\cos(\pi k_1)\sin(\pi k_1-2\pi k_1/L)/\sin(2\pi k_1/L)+L, \\
&= 2L(-1)^{k_1}(-1)^{k_1}\sin(-2\pi k_1/L)/\sin(2\pi k_1/L)+L, \\
&= -L. \qquad \text{(D.10)}
\end{aligned}
$$

Substituting Eq.(D.10) into Eq.(D.9), we have

$$\langle S^2(\mathbf{k})\rangle = 2A^2 - \frac{3A^2}{L^2} + \frac{B}{L^2}. \qquad \text{(D.11)}$$

We can now calculate the standard deviation σ_S of $S(\mathbf{k})$ as

$$
\begin{aligned}
\sigma_S &= \sqrt{\frac{1}{L^2}\sum(S(\mathbf{k})-\langle S(\mathbf{k})\rangle)^2}, \\
&= \sqrt{\langle S^2(\mathbf{k})\rangle - \langle S(\mathbf{k})\rangle^2}, \\
&= \begin{cases} \sqrt{A^2 - \dfrac{3A^2}{L^2} + \dfrac{B}{L^2}} & \text{if } \mathbf{k}\neq 0 \text{ or } \mathbf{k}\neq \dfrac{L}{2}\mathbf{i}+\dfrac{L}{2}\mathbf{j} \\ \sqrt{2A^2 - \dfrac{3A^2}{L^2} + \dfrac{B}{L^2}} & \text{if } \mathbf{k}=0 \text{ and } \mathbf{k}=\dfrac{L}{2}\mathbf{i}+\dfrac{L}{2}\mathbf{j} \end{cases} \qquad \text{(D.12)}
\end{aligned}
$$

Thus if we measure $S(\mathbf{k})$ $M(\mathbf{k})$ times, the standard deviation of the mean $\sigma_{\bar{S}}$ is

$$\sigma_{\bar{S}} = \frac{\sigma_S}{\sqrt{M(\mathbf{k})}}. \qquad \text{(D.13)}$$

Next let us consider some examples. We consider an order parameter randomly chosen to be $\phi = \pm 1$. We get $A = B = 1$. Thus

$$\sigma_S = \begin{cases} \sqrt{1-\dfrac{2}{L^2}} & \text{if } \mathbf{k}\neq 0 \text{ or } \mathbf{k}\neq \dfrac{L}{2}\mathbf{i}+\dfrac{L}{2}\mathbf{j} \\ \sqrt{2-\dfrac{2}{L^2}} & \text{if } \mathbf{k}=0 \text{ and } \mathbf{k}=\dfrac{L}{2}\mathbf{i}+\dfrac{L}{2}\mathbf{j} \end{cases} \qquad \text{(D.14)}$$

For an order parameter uniformly distributed between -1 and $+1$, we have

$$
\begin{aligned}
A &= \frac{1}{2}\int_{-1}^{1} x^2 dx = \frac{1}{3}, \\
B &= \frac{1}{2}\int_{-1}^{1} x^4 dx = \frac{1}{5}. \qquad \text{(D.15)}
\end{aligned}
$$

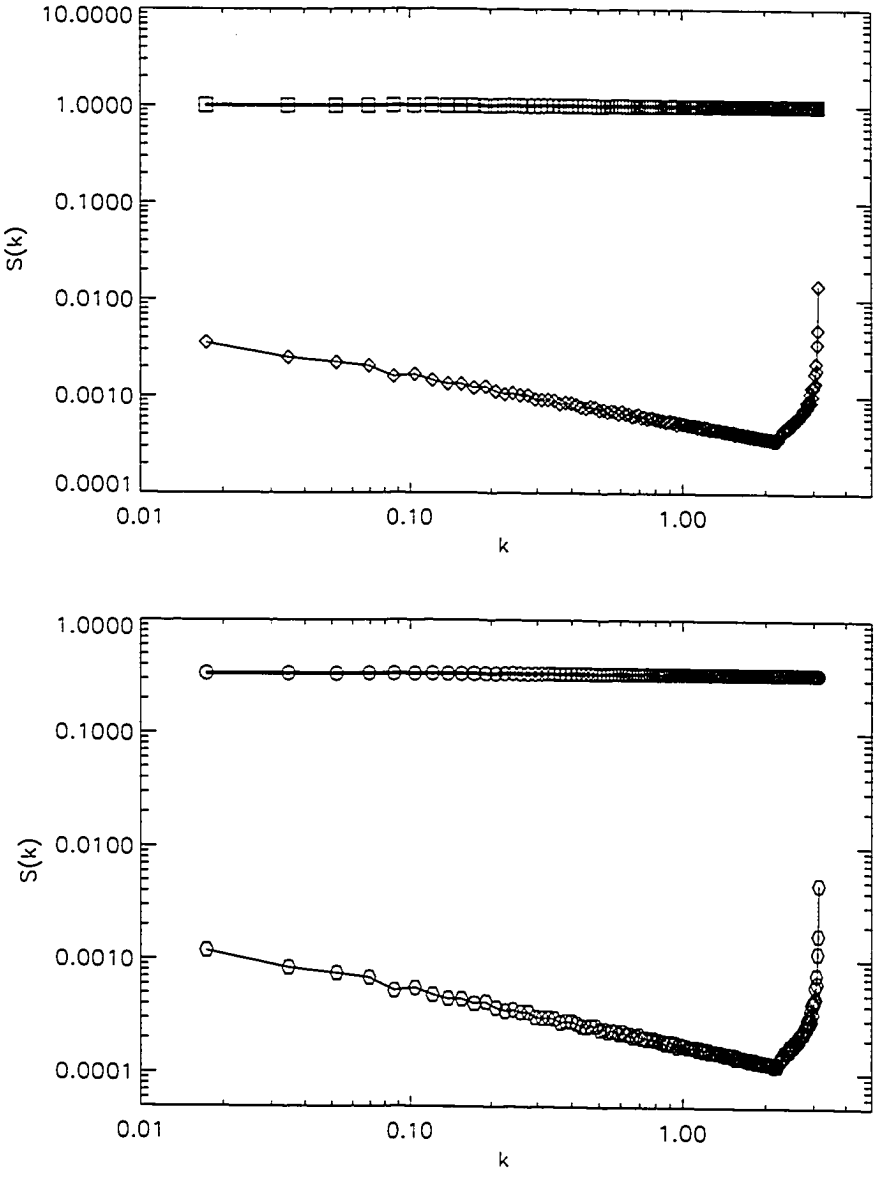

Figure D.1: Structure factor $S(k)$ vs k (open square in the upper figure for an order parameter ϕ randomly chosen to be either -1 or $+1$, open circle in the lower figure for an order parameter uniformly distributed between -1 and $+1$). The theoretical predicted averaged value is also plotted (thick solid line in both figures). The standard deviation of the mean of the structure factor $S(k)$ vs k is plotted too (open diamond in the upper figure, and open hexagon in the lower figure). The theoretical predicted averaged value $\sigma_{\bar{S}}$ (see Eq.(D.13)) is also plotted (thin solid line in both figures), where $M(k)$ is the times we average $S(k)$. The linear system size $L_{sys} = 256$. The data is obtained by averaging over 10000 systems.

Thus we have

$$\sigma_S = \begin{cases} \sqrt{\frac{1}{9} - \frac{2}{15L^2}} & \text{if } \mathbf{k} \neq 0 \text{ or } \mathbf{k} \neq \frac{L}{2}\mathbf{i} + \frac{L}{2}\mathbf{j} \\ \sqrt{\frac{2}{9} - \frac{2}{15L^2}} & \text{if } \mathbf{k} = 0 \text{ and } \mathbf{k} = \frac{L}{2}\mathbf{i} + \frac{L}{2}\mathbf{j} \end{cases} \tag{D.16}$$

and these are confirmed by the computational calculation with two different random generator ran2 and ran4 [28], and they give the same results, which is plotted with the theoretical predicted values in Fig.D.1. All the data in the figures are obtained using ran4.

Appendix E

Scaling of field derivatives in Fourier space

In order to study the accuracy of these accelerated algorithms, it is necessary to know the scaling of field derivatives in both real and Fourier space. Vollmayr-Lee and Rutenberg [27] have studied the scaling of field derivatives in real-space in order to study the single-step error. In this thesis, our analysis on accuracy of these accelerated algorithms are based on scaling of field derivatives in Fourier space.

We first consider conserved dynamics. Since

$$S(k) = \langle |\phi_k|^2 \rangle = L^2 g(kL), \tag{E.1}$$

where $g(kL) \sim (kL)^{-3}$ as $kL \gg 1$, we obtain

$$|\phi_k| \sim L\sqrt{g(kL)} \sim t_s^{1/3} \tag{E.2}$$

because $g(kL) = O(1)$ for $kL = O(1)$. Previous studies [1, 31] showed that

$$\dot{\phi}_k = \dot{L} k \phi_k \tag{E.3}$$

as $kL \gg 1$, so we have the form for the time-derivative correlation function as

$$T(k) = \langle |\dot{\phi}_k|^2 \rangle = \dot{L}^2 k^2 \langle |\phi_k|^2 \rangle = \dot{L}^2 h_1(kL), \tag{E.4}$$

where

$$h_1(kL) = k^2 L^2 g(kL) \sim (kL)^{-1} \tag{E.5}$$

as $kL \gg 1$ is the scaling function, and we have

$$|\dot{\phi}_k| \sim \dot{L}\sqrt{h_1(kL)} \sim t_s^{-2/3} \tag{E.6}$$

because $h_1(kL) = O(1)$ for $kL = O(1)$.

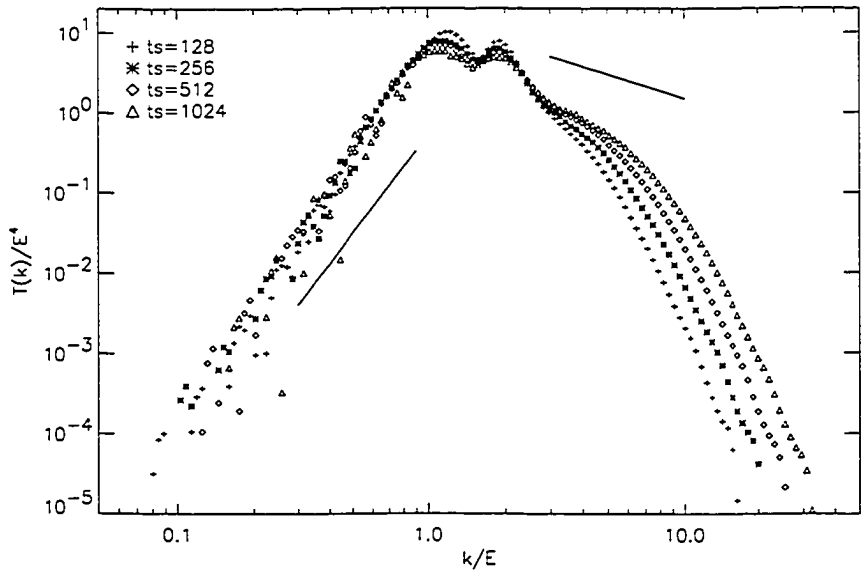

Figure E.1: Plot of $T(k)/E^4$ vs k/E for conserved systems, with Euler update, $\Delta t = 0.03$, $L_{sys} = 256$, averaged 15 samples. The two reference lines are $\sim x^4$ and $\sim x^{-1}$. Although as $kL \gg 1$, the data do not show precisely $T(k)/E^4 \sim (k/E)^{-1}$, we think it is due to finite time transients. For a larger system size and later times, we expect to confirm the relation in Eq.(4.29).

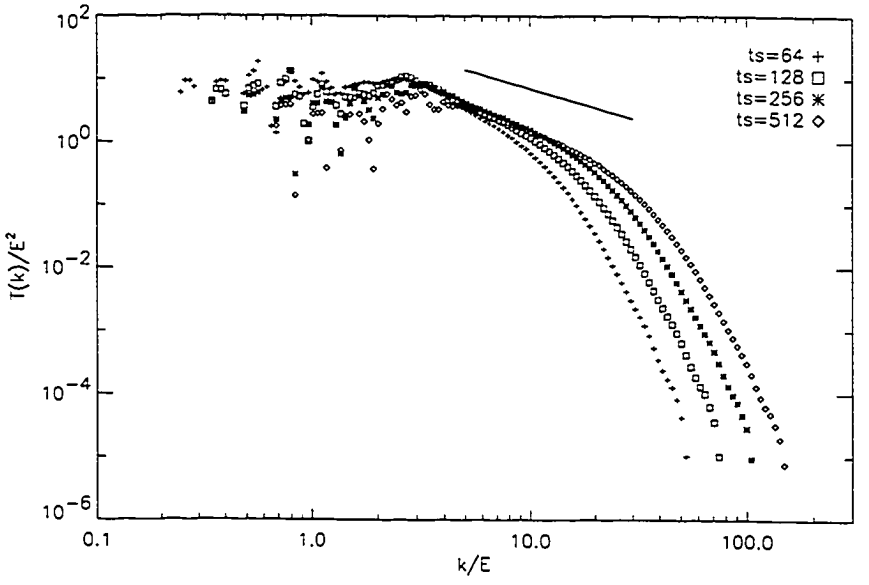

Figure E.2: Plot of $T(k)/E^2$ vs k/E for non-conserved systems, with Euler update, $\Delta t = 0.2$, $L_{sys} = 256$, averaged 15 samples. The reference line is $\sim x^{-1}$. Although as $kL \gg 1$, the data do not show precisely $T(k)/E^2 \sim (k/E)^{-1}$, we think it is due to finite time transients. For a larger system size and later times, we expect to confirm the relation in Eq.(4.77).

The time-derivative correlation function $T(k)$ have not been studied before. We measure $T(k)$ numerically and confirm the scaling of $h(x)$ in both conserved and non-conserved systems. See Fig.E.1 and Fig.E.2 for details.

The generalization of more time-derivative correlations for conserved two dimensional scalar order parameter is

$$\langle |\partial_t^n \phi_k|^2 \rangle \sim \dot{L}^2 k^2 \langle |\partial_t^{n-1} \phi_k|^2 \rangle, \tag{E.7}$$

where $\sim$ is used to indicate that LHS may not exactly equal to RHS.

Applying this relation will yield

$$\langle |\partial_t^n \phi_k|^2 \rangle \sim \dot{L}^{2n} L^{2-2n} h_n(kL), \tag{E.8}$$

where

$$h_n(kL) = k^2 L^2 h_{n-1}(kL) \sim (kL)^{2n-3} \tag{E.9}$$

as $kL \gg 1$. Note that as $n > 1$, $h_n(kL) \lesssim (L/\xi)^{2n-3} \sim t_s^{2n/3-1}$. It follows that

$$|\partial_t^n \phi_k| \sim \dot{L}^n L^{1-n} \sqrt{h_n(kL)} \sim t_s^{-2n/3-1/6} \tag{E.10}$$

for $n > 1$. To summary, we have

$$|\partial_t^n \phi_k| \sim \begin{cases} t_s^{-n+1/3} & n = 0, 1 \\ t_s^{-2n/3-1/6} & n > 1 \end{cases} \tag{E.11}$$

for conserved two dimensional scalar order parameter. For non-conserved two dimensional scalar order parameter, we can obtain similarly that

$$|\partial_t^n \phi_k| \sim \begin{cases} t_s^{-n+1/2} & n = 0, 1 \\ t_s^{-n/2-1/4} & n > 1 \end{cases} \tag{E.12}$$

Note that the scaling functions for non-conserved and conserved two dimensional scalar order parameter have the same behavior as $kL \gg 1$.

Eq.(E.11) and Eq.(E.12) are important relations we use in our accuracy analysis for accelerated algorithms.

Appendix F

Moments of correlations in conserved systems

Study of the moments of correlations looked like an interesting topic in understanding the structure of the coarsening systems. However they prove to have time dependence even in the scaling regime due to transients in the correlations.

The definition of nth moments of a function $f(x)$ is

$$M_n(x) = \int f(x)x^n dx. \tag{F.1}$$

In conserved systems, first, we want to predict what moments can be calculated for $S(k)$. Because $S(k) \sim k^4$ as k is small [46, 47] and $S(k) \sim k^{-3}$ as $1 \ll k \leq 1/\xi$ [29], we expect $S(k)$ has valid moments for $-4 \leq n \leq 2$.

It is interesting to predict the time-dependence of the moments of the correlation functions and structure factors. First, note that for a given time, $1/E \sim L \sim t_s^{1/3}$, $k_{min} \sim 1/L_{sys}$ and $k_{max} \sim 1/\xi$, where ξ is the domain wall width. Therefore, $(k/E)_{min} \sim t_s^{1/3}/L_{sys}$ and $(k/E)_{max} \sim t_s^{1/3}/\xi$. For the nth moments, we have

$$M_n = C + \int_{x_{min}}^{x_0} x^{n+4} dx + \int_{x_0'}^{x_{max}} x^{n-3} dx, \tag{F.2}$$

where x_0 is a constant in small k regime, x_0' is a constant in large k regime, C is a constant represents the integral between x_0 and x_0', and $x = k/E$. When $n \neq 2$ $(-4 \leq n \leq 1)$, we obtain

$$\begin{aligned} M_n &= C' - \frac{x_{min}^{n+5}}{n+5} + \frac{x_{max}^{n-2}}{n-2}, \\ &= C' - M\frac{t_s^{(n+5)/3}}{L_{sys}^{n+5}} + N\frac{t_s^{(n-2)/3}}{\xi^{n-2}}, \end{aligned} \tag{F.3}$$

where C' is a constant, M and N are prefactors. As late times, the third term $Nt_s^{(n-2)/3}/\xi^{n-2} \to 0$. For the second term, note that $L_{sys} \gg L(t_s) \sim t_s^{1/3}$, we get a small but non-zero time-dependent contribution in the moments. This has been confirmed by numerical studies (data not shown).

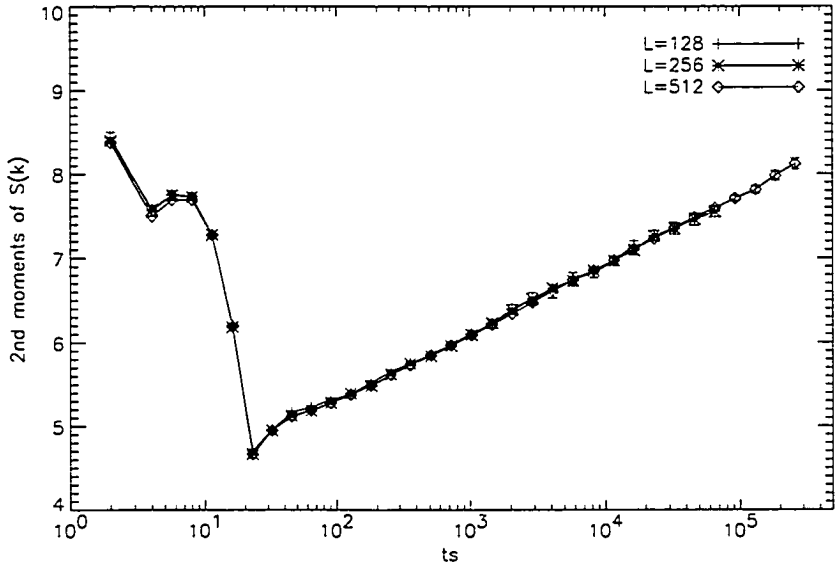

Figure F.1: Plot of M_2 ($\int S(k)k^2dk$) vs t_s for conserved systems, with Direct update, $\Delta t = 0.001t^{2/3}$, for three different system sizes $L_{sys} = 128$, 256 and 512. We see the linear increase of M_2 with respect to t_s. This confirms Eq.(F.5), which indicates that the slope is N'.

When $n = 2$, we obtain

$$\begin{aligned} M_2 &= C'' - \frac{x_{min}^7}{7} + \ln x_{max}, \\ &= C'' - M' \frac{t_s^{7/3}}{L_{sys}^7} + N' \ln t_s, \end{aligned} \tag{F.4}$$

where C'' is a constant, M' and N' are prefactors. At late times, the third term $N' \ln t_s$ dominates the integral. Therefore, we get

$$M_2 = N' \ln t_s, \tag{F.5}$$

at late times. Fig.F.1 confirms this prediction.

We see that these moments depend on time. Since we always want to study the time-independence of the correlations in coarsening systems, the moments appear not to be a good probe.

Appendix G

Asymmetric potentials for asymmetric bulk diffusivities

In the study of asymmetric bulk diffusivities generated by asymmetric potentials, the choices of selecting a suitable potential that agrees with Eq.(5.12) is not unique, even with the requirement that $V'(\phi_\pm) = 0$ at $\phi_\pm = \pm 1$. In this Appendix, we introduce some other forms of potential that may be of interest.

Chapter 5 introduced

$$V_1(\phi) = \frac{1}{8}(\phi^2 - 1)^2(\phi^2 + 2b\phi + 1), \tag{G.1}$$

which is $O(\phi^6)$. We can instead add terms to the symmetric potential $V_0(\phi) = (\phi^2 - 1)^2/4$. Probably the simplest is

$$V_2(\phi) = \frac{1}{4}(\phi^2 - 1)^2 + \frac{1}{3}b\phi^3 - b\phi, \tag{G.2}$$

with $b \in [0, 1]$, which yields

$$V_2'(\phi) = (\phi^2 - 1)(\phi + b). \tag{G.3}$$

This indicates that $V_2(\phi)$ has two global minima at $\phi_\pm = \pm 1$, and a local maximum at $\phi = -b$. Calculating $V_2''(\phi)$ gives

$$V_2''(\phi) = 3\phi^2 - 1 + 2b\phi. \tag{G.4}$$

We have $V_2''(\phi_\pm) = 2(1 \pm b)$, which agrees with Eq.(5.12).

The another choice is

$$V_3(\phi) = \frac{1}{4}(\phi^2 - 1)^2 + \frac{3}{20}b\phi^5 - \frac{1}{6}b\phi^3 - \frac{1}{4}b\phi, \tag{G.5}$$

with $b \in [0, 1]$, which yields

$$V_3'(\phi) = \frac{3}{4}b\phi^4 + \phi^3 - \frac{1}{2}b\phi^2 - \phi - \frac{1}{4}b. \tag{G.6}$$

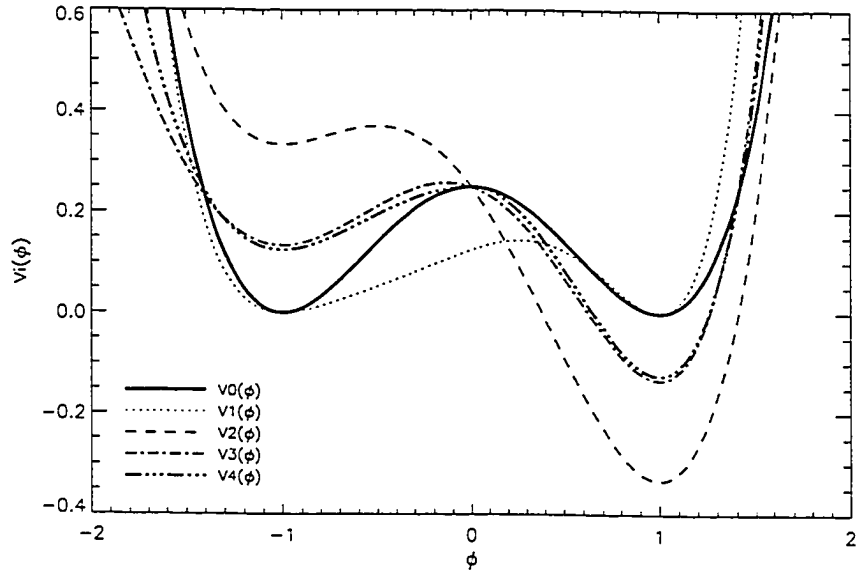

Figure G.1: Plot of different choices of potentials $V_i(\phi)$ vs ϕ for $b = 0.5$, together with the double-well potential $V_0(\phi) = (\phi^2 - 1)^2/4$.

This indicates that $V_3(\phi)$ has two global minima at $\phi_\pm = \pm 1$, and a local maximum. Calculating $V_3''(\phi)$ gives

$$V_3''(\phi) = (3\phi^2 - 1)(1 + b\phi). \tag{G.7}$$

We have $V_3''(\phi_\pm) = 2(1 \pm b)$, which agrees with Eq.(5.12).

The another choice is

$$V_4(\phi) = \begin{cases} \dfrac{1+b}{4}(\phi^2 - 1)^2 - \dfrac{b}{4} & \text{if } \phi \geq 0 \\ \dfrac{1-b}{4}(\phi^2 - 1)^2 + \dfrac{b}{4} & \text{if } \phi < 0 \end{cases} \tag{G.8}$$

with $b \in [0, 1]$. $V_4(\phi)$ is continuous at $\phi = 0$, and we have

$$V_4'(\phi) = \begin{cases} (1+b)(\phi^3 - \phi) & \text{if } \phi \geq 0 \\ (1-b)(\phi^3 - \phi) & \text{if } \phi < 0 \end{cases} \tag{G.9}$$

$V_4'(\phi)$ is also continuous at $\phi = 0$. We see that $V_4(\phi)$ has two global minima $\mp b/4$ at $\phi_\pm = \pm 1$ and a local maximum $1/4$ at $\phi = 0$. Calculating $V_4''(\phi)$ gives

$$V_4''(\phi) = \begin{cases} (1+b)(3\phi^2 - 1) & \text{if } \phi \geq 0 \\ (1-b)(3\phi^2 - 1) & \text{if } \phi < 0 \end{cases} \tag{G.10}$$

We have $V_4''(\phi_\pm) = 2(1 \pm b)$, which agrees with Eq.(5.12).

See Fig.G.1 for a comparison of these choices. For $V_1(\phi)$, the advantage is that it has equal-depth minima, but its disadvantage is also obvious — as the asymmetric parameter $b = 0$, $V_1(\phi) \neq V_0(\phi)$, also, the local maximum is at $\phi = 0$ only as $b = 0$. $V_2(\phi)$ and $V_3(\phi)$ are quite similar — their advantages are that as the asymmetric parameter $b = 0$, $V_2(\phi) = V_3(\phi) = V_0(\phi)$, but their disadvantage is that the local maximum is at $\phi = 0$ only as $b = 0$, and they do not have equal-depth shape. For $V_4(\phi)$, the advantage is that as the asymmetric parameter $b = 0$, $V_4(\phi) = V_0(\phi)$, and the local maximum is always at $\phi = 0$. The disadvantage is that this form is not analytic, and so may not be physically reasonable.

Bibliography

[1] A. J. Bray, "Theory of phase-ordering kinetics", Adv. Phys. **43**, 357 (1994).

[2] J. D. Gunton, M. San Miguel and P. S. Sahni, in *Phase Transitions and Critical Phenomena*, Vol. 8, edited by C. Domb and J. L. Lebowitz (New York Academic Press, 1983) pp. 267.

[3] H. Furukawa, "Dynamic scaling assumption for phase separation", Adv. Phys., **34**, 703 (1985).

[4] J. S. Langer, in *Solids far from Equilibrium*, edited by C. Godrèche (Cambridge University Press, 1992), pp. 297.

[5] P. Wiltzius and A. Cumming, "Domain growth and wetting in polymer mixtures", Phys. Rev. Lett. **66**, 3000 (1991).

[6] R. F. Shannon, S. E. Nagler, C. R. Harkless and R. M. Nicklow, "Time-resolved x-ray-scattering study of ordering kinetics in bulk single-crystal Cu_3Au", Phys. Rev. B **46**, 40 (1992).

[7] B. D. Gaulin, S. Spooner and Y. Morii, "Kinetics of phase separation in $Mn_{0.67}Cu_{0.33}$", Phys. Rev. Lett. **59**, 668 (1987).

[8] N. Mason, A. N. Pargellis and B. Yurke, "Scaling behavior of two-time correlations in a twisted nematic liquid crystal", Phys. Rev. Lett. **70**, 190 (1993).

[9] I. Chuang, N. Turok and B. Yurke, "Late-time coarsening dynamics in a nematic liquid crystal", Phys. Rev. Lett. **66**, 2472 (1991).

[10] P. Laguna and W. H. Zurek, "Density of Kinks after a Quench: When Symmetry Breaks, How Big are the Pieces?", Phys. Rev. Lett. **78**, 2519 (1997).

[11] A. J. Bray, "Renormalization-group approach to domain-growth scaling", Phys. Rev. B **41**, 6724 (1990).

[12] J. W. Cahn and J. E. Hilliard, "Free energy of a nonuniform system. I. Interface free energy", J. Chem. Phys. **28**, 258 (1958).

[13] M. Hennion, D. Ronzaud and P. Guyot, "Kinetics of unmixing in Al-Zn single crystals studied by neutron small angle scattering", Acta Metall. **30**, 599 (1982).

[14] J. Marro, J. L. Lebowitz, and M. H. Kalos, "Computer Simulation of the Time Evolution of a Quenched Model Alloy in the Nucleation Region", Phys. Rev. Lett. **43**, 282 (1979).

[15] R. B. Griffiths, "Dependence of Critical Indices on a Parameter", Phys. Rev. Lett. **24**, 1479 (1970).

[16] P. C. Hohenberg and B. I. Halperin, "Theory of dynamic critical phenomena", Rev. Mod. Phys. **49**, 435 (1977).

[17] R. Ahluwalia, "Phase separation in a simple model with dynamical asymmetry", Phys. Rev. E **59**, 263 (1999).

[18] S. Puri, A. J. Bray, and J. L. Lebowitz, "Phase-separation kinetics in a model with order-parameter-dependent mobility", Phys. Rev. E **56**, 758 (1997).

[19] T. M. Rogers, K. R. Elder and R. C. Desai, "Numerical study of the late stages of spinodal decomposition", Phys. Rev. B **37**, 9638 (1988).

[20] Y. Oono and S. Puri, "Study of phase-separation dynamics by use of cell dynamical systems. I. Modeling", Phys. Rev. A **38**, 434 (1998).

[21] L. Q. Chen and J. Shen, "Applications of semi-implicit Fourier-spectral method to phase field equations", Comput. Phys. Commun. **108**, 147 (1998).

[22] J. Zhu, L. Q. Chen, J. Shen and V. Tikare, "Coarsening kinetics from a variable-mobility Cahn-Hilliard equation: Application of a semi-implicit Fourier spectral method", Phys. Rev. E **60**, 3564 (1999).

[23] A. Shinozaki and Y. Oono, "Spinodal decomposition in 3-space", Phys. Rev. E **48**, 2622 (1993).

[24] M. Zapotocky, P. M. Goldbart and N. Goldenfeld, "Kinetics of phase ordering in uniaxial and biaxial nematic films", Phys. Rev. E **51**, 1216 (1995).

[25] D. J. Eyre, "An Unconditionally Stable One-Step Scheme for Gradient Systems", http://www.math.utah.edu/~eyre/research/methods/stable.ps

[26] D. J. Eyre, in *Computational and Mathematical Models of Microstructural Evolution*, edited by J. W. Bullard *et al.* (The Material Research Society, Warrendale, PA, 1998), pp. 39-46.

[27] B. P. Vollmayr-Lee and A. D. Rutenberg, "Fast and accurate coarsening simulation with an unconditionally stable time step", Phys. Rev. E **68**, 66703 (2003).

[28] W. H. Press, S. A. Teukolsky, W. T. Vetterling, and B. P. Flannery, *Numerical Recipes in C*, 2nd Ed. (Cambridge University Press, New York, 1993).

[29] G. Porod, in *Small Angle X-Ray Scattering*, edit by O. Glatter and L. Kratky (Academic, New York, 1983).

[30] A. J. Bray and A. D. Rutenberg, "Growth laws for phase ordering", Phys. Rev. E **49**, R27 (1994).

[31] A. D. Rutenberg and A. J. Bray, "Energy-scaling approach to phase-ordering growth laws", Phys. Rev. E **51**, 5499 (1995).

[32] M. Cheng and A. D. Rutenberg, "Maximally-fast coarsening algorithms", submitted, (http://arxiv.org/abs/cond-mat/0507033).

[33] Y. Mao, T. C. B. McLeish, P. I. C. Teixeira and D. J. Read, "Asymmetric landscapes of early spinodal decomposition", Eur. Phys. J. E **6**, 69 (2001).

[34] D. A. Huse, "Corrections to late-stage behavior in spinodal decomposition: Lifshitz-Slyozov scaling and Monte Carlo simulations", Phys. Rev. B **34**, 7845 (1986).

[35] M. Siegert, "Growth dynamics with an anisotropic surface tension", Phys. Rev. A **42**, 6268 (1990).

[36] A. D. Rutenberg, "Stress-free spatial anisotropy in phase ordering", Phys. Rev. E **54**, R2181 (1996).

[37] A. D. Rutenberg and B. P. Vollmayr-Lee, "Anisotropic Coarsening: Grain Shapes and Nonuniversal Persistence", Phys. Rev. Lett. **83**, 3772 (1999).

[38] G. Caginalp and P. Fife, "Higher-order phase field models and detailed anisotropy", Phys. Rev. B **34**, 4940 (1986).

[39] J. W. Cahn and R. Kikuchi, "Transition layer in a lattice-gas model of a solid-melt interface", Phys. Rev. B **31**, 4300 (1985).

[40] P. R. Harrowell and D. W. Oxtoby, "On the interaction between order and a moving interface: Dynamical disordering and anisotropic growth rates", J. Chem. Phys. **86**, 2932 (1987).

[41] G. Caginalp, "The role of microscopic anisotropy in the macroscopic behavior of a phase boundary", Ann. Phys. (N.Y.) **172**, 136 (1986).

[42] R. Kobayashi, "Modeling and numerical simulations of dendritic crystal growth", Physica D **63**, 410 (1993).

[43] A. A. Wheeler, B. T. Murray and R. J. Schaefer, "Computation of dendrites using a phase field model", Physica D **66**, 243 (1993).

[44] J. J. Eggleston, G. B. McFadden and P. W. Voorhees, "A phase-field model for highly anisotropic interfacial energy", Physica D **150**, 91 (2001).

[45] J. A. Warren, W. J. Boettinger, "Prediction of dendritic growth and microsegregation patterns in a binary alloy using the phase-field method", Acta Metall. Mater. **43**, 689 (1995).

[46] C. Yeung, "Scaling and the Small-Wave-Vector Limit of the Form Factor in Phase-Ordering Dynamics", Phys. Rev. Lett. **61**, 1135 (1988).

[47] H. Furukawa, "Comment on 'Scaling and the smallwave-vector limit of the form factor in phase-ordering dynamics'." Phys. Rev. Lett. **62**, 2567 (1989).